University of Bucharest - Faculty of Physics

Gamma spectroscopy following the beta-decay of neutron rich nuclei at ISOLDE

Master Thesis

Răzvan Lică

Coordinators:
Dr. Nicolae Marius Mărginean, *IFIN-HH*
Prof. Dr. Octavian Sima, *FFUB*

– 2014 –

Acknowledgements

I express my gratitude for the support and guidance of Dr. Nicolae Marius Mărginean. I also thank all my professors from the Faculty of Physics, especially Prof. Dr. Octavian Sima who offered his assistance and support in preparing my Masters Thesis. In addition, I would like to thank all the participants of the ISOLDE IS441 experiment, particularly Dr. Henryk Mach, Dr. Luis Fraile and Dr. Gary Simpson for their contribution to the experiment and present work.

Contents

1 Nuclear structure models **3**

1.1 Historical Overview 3

1.2 Spherical shell model 5

1.3 Deformed shell model 9

2 Nuclear structure observables **15**

2.1 Spin and parity of nuclear levels 15

2.2 Properties of gamma decay 18

2.2.1 Energy conservation 18

2.2.2 Spin and parity conservation 19

2.2.3 Transition probabilities 20

2.2.4 Branching ratio 24

2.2.5 Internal conversion 24

2.3 Properties of beta decay 27

2.3.1 Decay lifetimes and logft values 28

2.3.2 Selection rules for beta decay 30

3 Gamma spectroscopy of ^{80}Ga following the β-decay of ^{80}Zn **31**

3.1 Scientific motivation 31

3.2 The ISOLDE facility and the IS441 experimental setup 32

3.3 Experimental results 36

3.3.1 Improved level scheme. Absolute gamma intensities 36

3.3.2 Nanosecond isomer identification 43

3.3.3 Conversion coefficient and multipolarity assignment for the 74.8 keV transition 44

3.3.4 Spin and parity assignments 45

3.4 Comparison with Shell-Model calculations 45

Bibliography **51**

Introduction

The recent development of Radioactive Ion Beam Facilities (RIB) [1] triggered a renewed interest in studying nuclear structure far from stability by producing and measuring exotic beams close to the neutron and proton drip lines. These far-from-stability nuclei exhibit some properties unpredicted by the standard nuclear structure models. Understanding such exotic phenomena is crucial in order to construct more elaborate and unified models with an improved predicting power.

In the present paper I will discuss the gamma spectroscopy study of ^{80}Ga following the beta decay of ^{80}Zn produced at the ISOLDE facility of CERN, Geneva, Switzerland. This measurement was part of the IS441 experiment which took place in 2009 and 2011 and was dedicated to systematic ultra-fast timing studies of neutron-rich Zn nuclei.

In the first chapter I will present some of the most important aspects of the nuclear Shell Model. The second chapter is a brief overview of the observables significant for studying nuclear structure in the single-particle Shell Model framework, required in understanding the results which make the object of this thesis. Part of the theoretical background is based on [2].

For my Bachelor Degree, I presented the offline data-sorting algorithm which I developed in order to interpret the ^{80}Zn beta-decay data collected during the 2009 run of the IS441 experiment. In the third chapter I will present the results I obtained from both 2009 and 2011 runs of the experiment. By using the data-sorting algorithm I was able to create event-lists readable by the GaspWare dedicated analysis software. This allowed me to build γ-singles spectra and $\beta - \gamma(t) - \gamma(t)$ coincidence matrices for both HPGe and $LaBr_3$:Ce detectors in order to extract fast-timing information or investigate transition placement inside the level schemes. At the end of the chapter I present a comparison between the measured observables and shell-model calculations using two widely used interactions for this region, jj44bpn and JUN45. The calculations were performed by Dr. Gary Simpson with the NuShellX@MSU program and were verified by myself with the Antoine code using the JUN45 interaction.

Chapter 1

Nuclear structure models

1.1 Historical Overview

Humankind wondered about the structure of matter since the ancient Greek philosophers, among which Democritus (c. 460 - c. 370 BC), influenced by his mentor Leucippus, postulated for the first time that everything is composed of "atoms" which are physically indivisible. For more than 2000 years no breakthrough was made to support this idea until the English chemist, meteorologist and physicist John Dalton enunciated the Gas Laws based on the assumption that atoms combine into molecules.

The discovery of the electron in 1897 by the British physicist Sir Joseph John Thomson was the first evidence that atoms have internal structure and he proposed the Thompson atomic model (also called "plum pudding" model) that explained the electrical neutrality of matter by placing electrons inside a sphere of positive charge. Albert Einstein brought the first empirical evidence for the atomic theory by interpreting the Brownian Motion of polen grains and publishing his finding in 1905 in the "Annus Mirabilis" papers [3].

In parallel with the development of atomic theory, the French physicist Antoine Henri Becquerel discovered radioactivity in 1896 by observing how a uranium salt would impress a photographic plate even if it was kept in darkness, and discovered thorium, polonium and radium helped by his doctoral students Marie Sklodowska-Curie and her husband Pierre Curie. The radiation emitted by the radioactive elements was later classified by the British physicist Ernest Rutherford, known as the father of nuclear physics. The classification was based on the penetration distance: alpha (the shortest), beta and gamma. His most notable experiment was the Gold Foil experiment [4] performed in 1909 in which his students, Hans Geiger and Ernest Marsden bombarded a thin gold foil with alpha particles produced by a radium source and detected some of the particles at backwards angles. The experimental setup is shown in Fig. 1.1. The Thompson model could not predict this, and Rutherford published in 1911 a paper which explained his finding and established the Rutherford Atomic Model in which the negatively charged electrons would orbit a positively charged nucleus.

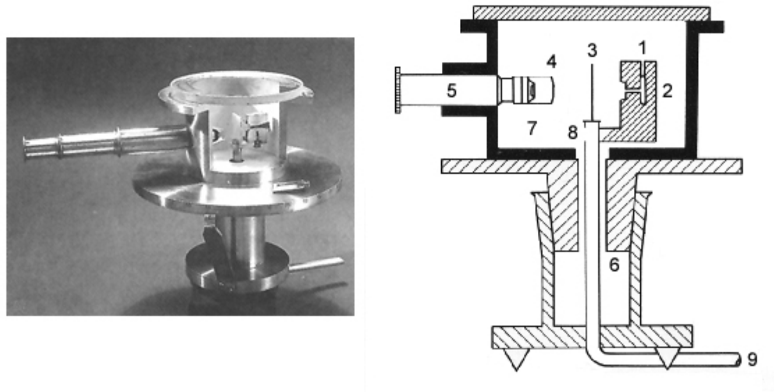

Figure 1.1: Photo and cross-section of the original apparatus of Rutherford, Geiger and Marsden: collimator (1), a-particle source (2), metal foil (3), scintillation screen (4), microscope (5), fitting (6), vacuum chamber (7), hole (8) and tube (9). [Source: Grehn, Metzler Physik; Demtröder, Experimentalphysik 3]

The internal constituents of the nucleus were unknown even though Rutherford noted a disparity between the atomic number of an atom and its atomic mass which could be explained by the existence of a neutrally charged particle within the atomic nucleus but he viewed it as a electron-proton pair. The experimental discovery of the neutron as we know it today was made in 1932 by the British physicist Sir James Chadwick who placed a polonium source near a beryllium target and producing an unknown form of radiation at that time which displaced protons from a paraffin wax [5].

Once it was established that the atomic nucleus is made of neutrons and protons, physicists elaborated various models for describing the forces that keep the nucleons together. At first, the nucleus was viewed as an incompressible liquid, the "Liquid drop" model, proposed by the Russian physicist George Gamow. Based on this model, Carl Friedrich von Weizsäcker and Hans Bethe in 1935 [6] introduced the semi-empirical mass formula which was successful in predicting nuclear radii and binding energies for most nuclei. Nevertheless, it was unable to predict a "magic" class of nuclei with enhanced stability compared to their neighbors.

Experimental measurements established the nuclear magic numbers 2, 8, 20, 28, 50, 82, 126 which represented the number of neutrons and protons for which the enhanced stability occurred. This suggests an internal shell structure for the nucleus similar with the atomic shell structure. The model was developed in 1949 through the independent work of several physicists, most notable being Eugene Paul Wigner and Maria Goeppert-Mayer.

It must be noted that at the present time there is no model capable to describe the nuclear structure as accurately as in the case of atomic structure due to the fact that the nuclear force is more complex than the electromagnetic force and is more difficult to probe. There has been made remarkable progress in improving single-particle and collective models in order to fit experimental data and we have a good understanding of nuclei near the stability line. Most of the problems appear as we approach the drip lines and physicist propose more complicated models, for example taking into account 3-body forces [7] as in QCD, in order to explain the behavior of exotic nuclei.

1.2 Spherical shell model

The atomic shell model explains the periodicity of chemical and physical properties and the fact that elements having the atomic number 2, 10, 18, 36, 54, 86 have an increased stability, forming the group of noble gases. The main conditions that must be satisfied in order to have this shell structure are:

1. In a first approximation it is considered that electrons move as independent particles in the attractive point-like coulombian field of the nucleus.
2. Reciprocal interaction between electrons is very small and is treated as a perturbation.
3. Electrons obey the Fermi-Dirac distribution.

At a first glance, the only similarity between the nucleus and the atom is that nucleons and electrons are fermions governed by the Fermi-Dirac statistics. Inside the nucleus we assumed a constant density such that we cannot discuss about an attractive center. Also, reciprocal interaction between nucleons is the attraction force which holds the nucleus together and cannot be disregarded. These simple observations clearly forbid a shell model interpretation of the nuclear structure and plead in favor of the collective models.

The study of static and dynamic properties of nuclei evidenced a certain periodicity regarding the number of protons and neutrons, similarly with atomic physics where the electrons are placed in certain shells around the nucleus. The nuclear magic numbers are 2, 8, 20, 28, 50, 82, 126. There is a staggering experimental evidence supporting these magic numbers, one of them being the natural abundances of certain isotopes having these specific numbers of protons or neutrons. Another is the excitation energy of the first 2+ state in even-even nuclei as shown in Fig. 1.2. Based on the analogy with atomic physics, it is clear that we need more energy to excite a nucleon between two shells than to excite it inside the same shell. In the case of magic nuclei, the first excited state can be achieved by an inter-shell excitation.

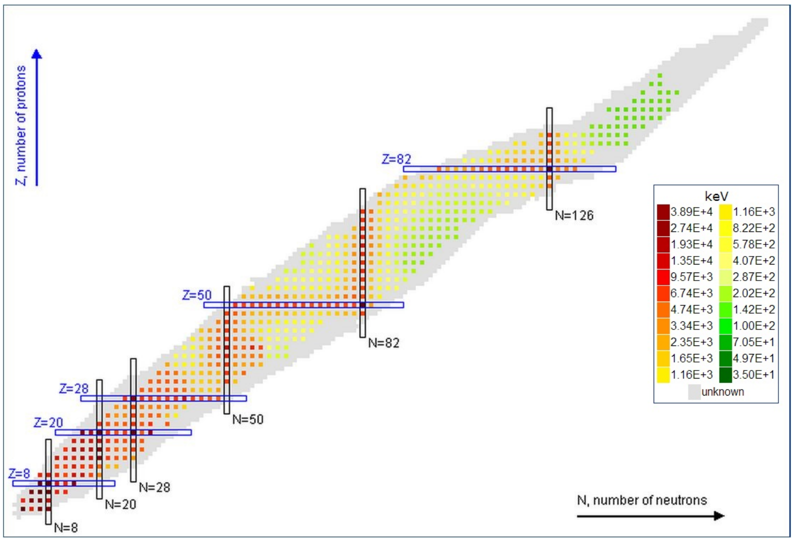

Figure 1.2: Excitation energy of the first 2^+ state. Figure taken from NNDC.

To construct the nuclear shell model in agreement with the experimental evidence we need to make the following hypothesis:

1. The bi-particle interaction between nucleons can be summed as a central interaction.

2. Inside the central field, the nucleons move independently.

We will discuss only about the single-particle shell model, which is a simpler but still efficient version of the nuclear shell model where we neglect the residual interaction between nucleons. The only interaction we consider is between each independent nucleon and the central mean-field. To reproduce the experimental magic numbers, the central potential (Fig. 1.3) must be described by the following formula:

$$V = -V_0 f(r, R_0, a) + b\vec{l}\vec{s}V_0 \frac{1}{r}\frac{d}{dr} f(r, R_0, a) + V_{Coul.}$$

where the potential well shape is described by the Woods-Saxon form factor

$$f(r, R_0, a) = \frac{1}{1 + e^{\frac{r - R_0}{a}}}$$

and we have the Coulomb repulsion term for the protons

$$V_{Coul.} = \begin{cases} \frac{(Z-1)e^2}{2R_0}(3 - (\frac{r}{R_0})^2) & \text{for} \quad r \leq R_0 \\ \frac{(Z-1)e^2}{r} & \text{for} \quad r > R_0 \end{cases}$$

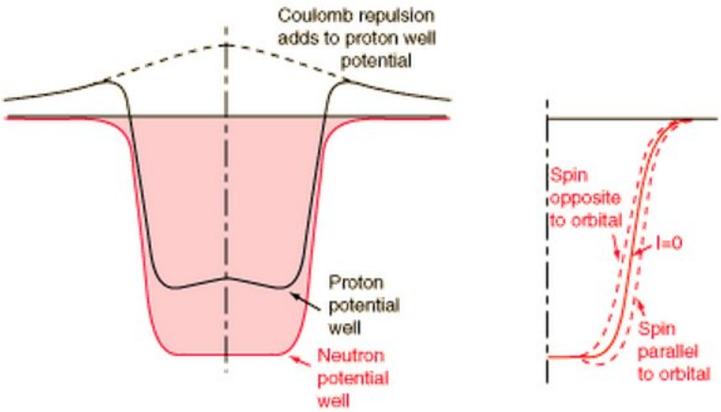

Figure 1.3: Qualitative representation of the potential well corresponding to the neutron and proton self-consistent field. Only the protons are affected by the Coulomb field. Figure taken from [8].

By neglecting the spin-orbit and Coulomb interactions and considering only the central potential V_i where the orbital angular momentum $\vec{l}$ is conserved, we have the following Hamiltonian:

$$H_0(i) = T_i + V_i = -\frac{\bar{h}^2}{2m_i}\Delta_i + V_i$$

By solving the Schrödinger equation

$$H_0(i)\psi(i) = E\psi(i)$$

we obtain the single-particle energies $E_{nl}^{(i)}$ which have a radial symmetry and depend on the radial quantum number n and orbital quantum number l. If we consider a harmonic oscillator potential well, we obtain the following magic numbers: $2, 8, 20, 40, 70, 112, \ldots$

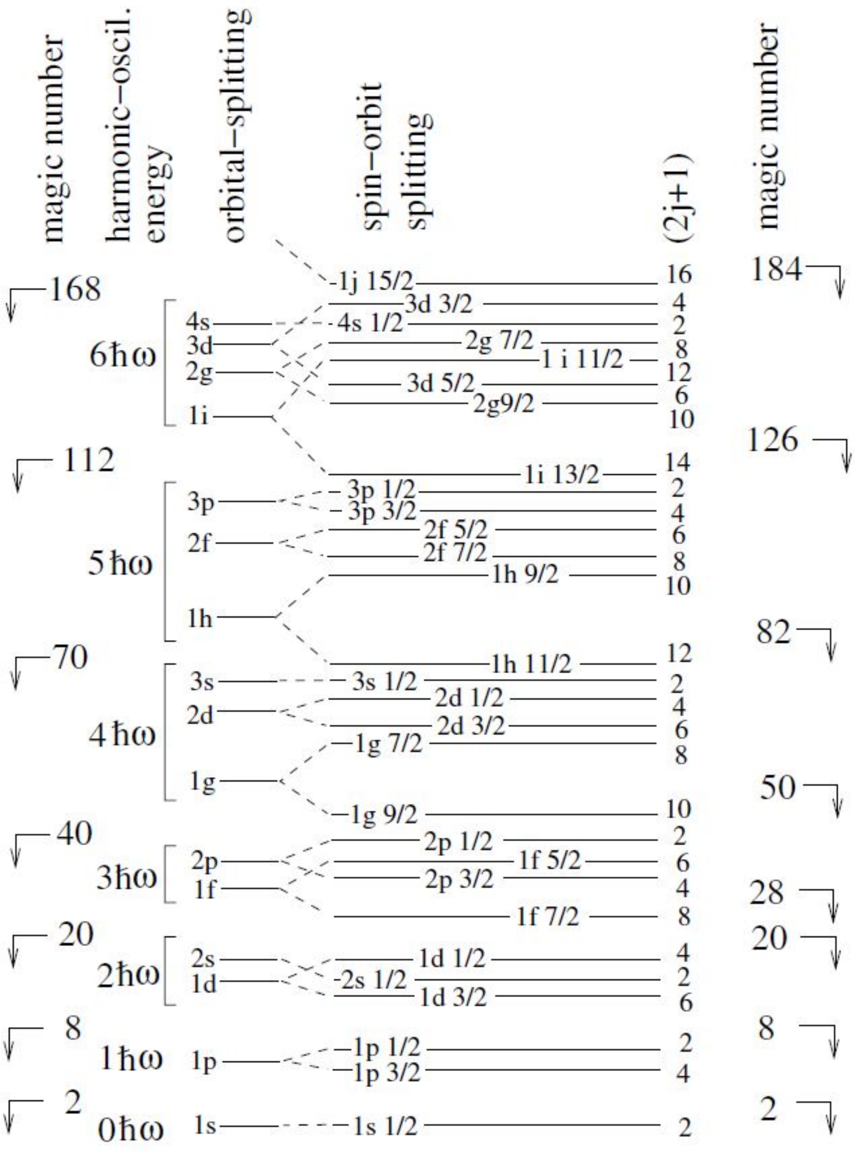

Figure 1.4: Nucleon orbitals in a model with a spin-orbit interaction. The two left-most columns show the magic numbers and energies for a pure harmonic potential. Figure taken from [9]

The spin-orbit interaction was introduced in 1949 by M.G. Mayer and independently O. Haxel, J.D. Jensen and H. Suess as an addition to the central mean field in order to reproduce the experimental magic numbers. The total angular momentum $\vec{j}$ is defined as the sum of the orbital angular momentum $\vec{l}$ and the intrinsic spin of the nucleon $\vec{s}$. We should also note that $|\vec{s}| = 1/2$ and for $l = 0, 1, 2, 3, 4, 5, 6, ...$ corresponds the $s, p, d, f, g, h, i, ...$ notations. The single particle (i) spin orbit (so) Hamiltonian can be written as:

$$H_{so}(i) = V_{so}^{(i)}(r)\vec{l}\vec{s} = \frac{1}{2}(\vec{j}^2 - \vec{l}^2 - \vec{s}^2)V_{so}^{(i)}(r)$$

The outcome is that a new degree of degeneracy is introduced, depending on the alignment between the spin and orbital momentum. Each level having a fixed orbital momentum l will gain $2(2l+1)$ degeneracy, each sublevel characterised by the total angular momentum $j = l \pm 1/2$. The previously deduced single particle levels $E_{nl}^{(i)}$ are split into $E_{nlj}^{(i)}$ as shown in Fig. 1.4. Introducing the radial functions $R_{nl}^{(i)}$ we can find the expectation values

$$\begin{aligned} E_{nl}^{(i)} &= \langle R_{nl}^{(i)}|H_0(i)|R_{nl}^{(i)}\rangle \quad \text{(similar to neglecting the spin-orbit interaction)} \\ \varepsilon_{nl}^{(i)} &= \langle R_{nl}^{(i)}|V_{so}^{(i)}(r)|R_{nl}^{(i)}\rangle \quad \text{(energy splitting difference)} \end{aligned}$$

We get the spin-orbit splitting single particle energy levels

$$E_{nlj}^{(i)} = \begin{cases} E_{nl}^{(i)} + \frac{1}{2}\varepsilon_{nl}^{(i)} l & \text{if} \quad j = l + 1/2 \\ E_{nl}^{(i)} - \frac{1}{2}\varepsilon_{nl}^{(i)}(l+1) & \text{if} \quad j = l - 1/2 \end{cases}$$

The single-particle shell model is very successful in predicting spins and parities for ground and excited states for many spherical nuclei without the need for introducing the residual interaction. It also explains the selection rules for gamma transitions, but this will be discussed in Chapter 3.

1.3 Deformed shell model

The spherical shell model does not have the prediction power to describe successfully nuclei having a permanently deformed ground state configuration. This is expected due to the fact that previously we considered a spherical symmetry for the central mean field. The surface of a deformed nucleus is most probably an ellipsoid, thus we can describe the radius by

$$R(\theta) = R_0(1 + \beta Y_{20}(\theta))$$

where β is the deformation coefficient (parameter).

The deformed shell model is based on the same mathematical approach as the spherical shell model, the only difference is the Woods-Saxon form factor that must contain $R(\theta)$ instead of R_0 and considering a small β.

$$f(r, R(\theta), a) = \frac{1}{1 + e^{\frac{r-R(\theta)}{a}}} = \frac{1}{1 + e^{\frac{r-R_0}{a}} e^{\frac{R_0 \beta Y_{20}}{a}}} \approx f(r, R_0, a) - R_0 \beta Y_{20} \frac{d}{dr} f(r, R_0, a)$$

The deformed self-consistent potential has the following expression

$$\begin{aligned}
V &= -V_0 f(r, R(\theta), a) + b\vec{l}\vec{s} V_0 \frac{1}{r}\frac{d}{dr} f(r, R(\theta), a) + V_{Coul.} \\
&= -V_0 f(r, R_0, a) + b\vec{l}\vec{s} V_0 \frac{1}{r}\frac{d}{dr} f(r, R_0, a) + \\
&\quad + V_0 R_0 Y_{20} \frac{d}{dr} f(r, R_0, a) - b\vec{l}\vec{s} V_0 R_0 \beta Y_{20} \frac{d^2}{r dr^2} f(r, R_0, a) + \\
&\quad + V_{Coul.}
\end{aligned}$$

The Schrödinger equation can only be solved numerically in order to obtain the single-particle spectra shown in Fig. 1.7. The total angular momentum j is not a "good" quantum number anymore, as it was the case of the orbital angular momentum after we introduced the spin-orbit interaction.

In the case of an elliptically deformed nucleus, the total angular momentum describes a precession around the symmetry axis z as shown in Fig. 1.5. The mean-value of the perpendicular component is zero, so the only observable is the longitudinal component K. This new quantum number can take 2j+1 values between $-j$ and j. Due to the reflection symmetry, states with spin projection K and -K will have the same energy, so we conclude that K will take $(2j + 1)/2$ values:

$$K = 1/2, 3/2, ..., j - 1, j$$

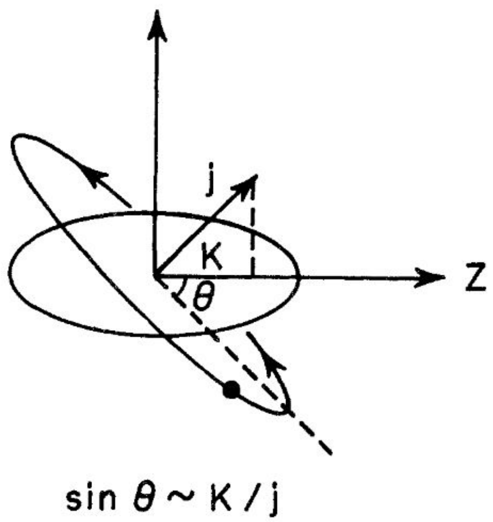

Figure 1.5: Schematic representation of the total angular momentum projection. Figure taken from [10]

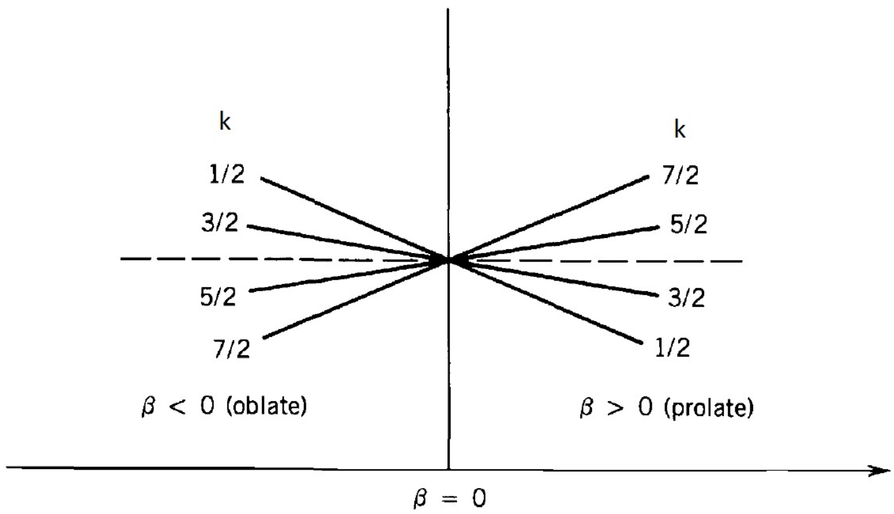

Figure 1.6: Energy splitting of the $l_j = f_{7/2}$ orbital into $(2j+1)/2 = 4$ sub-levels characterized by the new quantum number k in the case of an oblate and a prolate deformation. Figure taken from [11]

The parity will be given by the same formula $(-1)^l$. Numerical calculations show that for the prolate nuclei ($\beta > 0$) a high K sub-level will have a higher energy and it is the opposite for the oblate nuclei (($\beta < 0$). This is shown in Fig. 1.6. To evaluate the energetic spectra of a deformed nucleus, one must extract the deformation parameter β from the experimental measurement of the electric quadrupole moment.

The single-particle deformed shell model also disregards the residual interaction and cannot make correct predictions for even-even or odd-odd nuclei without making the same additional hypothesis as in the case of the spherical shell model. If we consider the case of large deformations the levels can rearrange such that new "magic" numbers will appear and will result permanently deformed ground states for nuclei having that specific deformation.

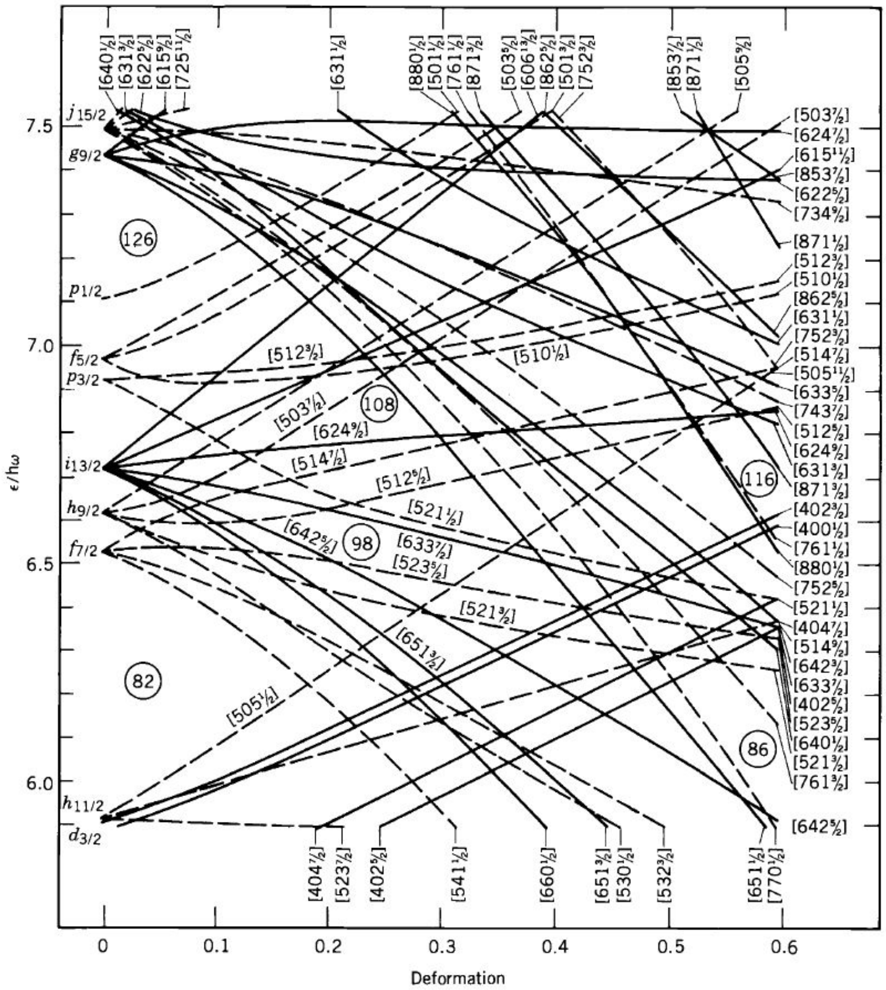

Figure 1.7: Energy diagram showing the splitting of the single particle levels as a function of the deformation parameter. Figure taken from [11]

Chapter 2

Nuclear structure observables

2.1 Spin and parity of nuclear levels

The single-particle shell model can predict spins and parities for ground states and excited states for many nuclei in agreement with the experimental measurements. There are different considerations that have to be taken into account for even-even, odd-odd and odd-even nuclei, although the main hypothesis is that only the unpaired nucleon influences nuclear properties such as spins, electric and magnetic moments, transition probabilities. It is often named a "valence" nucleon. The rest of the paired nucleons form an inert core that has total spin $I = 0$. This can be proven by considering the residual interaction for an even number of nucleons. The total energy of the configuration will be minimal when the nucleons pair up such that the intrinsic spins will cancel each other resulting in a total spin $I = 0$.

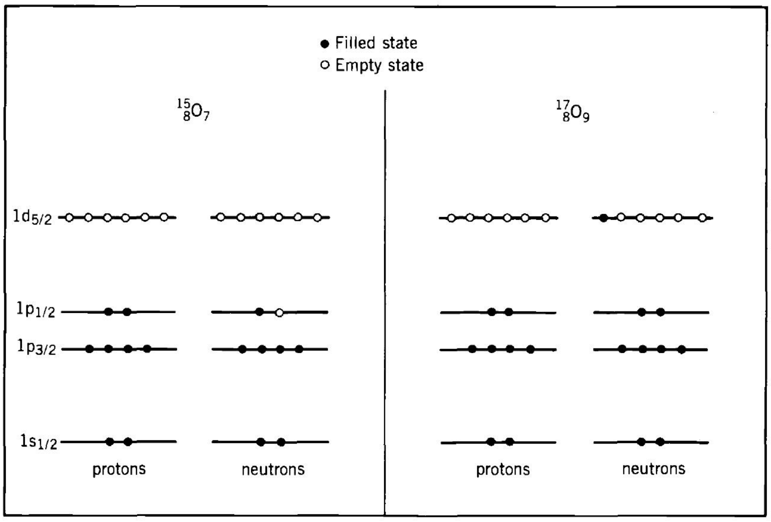

Figure 2.1: Schematic representation of the shell filling for ^{16}O and ^{17}O. The filled proton shells do not contribute to the structure. Figure taken from [11].

Even-Even nuclei

The single-particle assumption is based on the experimental evidence that even-even nuclei have spin $I = 0$ ground states. There is no exception for this observation. Excited levels are obtained by one or more nucleons going on higher single-particle states. If there is a full shell occupancy, the next excited state will have a higher energy because of the large inter-shell gap. This is how we can explain the large excitation energy of the first excited state of the double magical nuclei compared to the neighbouring nuclei.

Odd-even nuclei

In this case, the ground state spin is equal to the angular momentum j of the unpaired nucleon and the parity of the ground state is $(-1)^l$. This rule is valid for most of the known nuclei except some cases around mass $A = 20$ and for heavier masses for which:

$$
\begin{aligned}
63 \leq Z \leq 73; \quad Z \geq 89 \\
89 \leq N \leq 107; \quad N \geq 141
\end{aligned}
$$

The reason is that in most of these exceptions the electric quadrupole moment is different from zero meaning that nuclei in these regions are deformed and the present model is inadequate. Nevertheless, some of the exceptions are represented by spherical nuclei and the explanation is related to the strong pairing effects.

The first excited states in odd-even nuclei are usually represented by the excitation of the unpaired nucleon. If we have a single outer shell nucleon, we can neglect the residual interaction, as it is the example of $^{17}_{8}O$ (one neutron in $1d_{5/2}$). If we have more nucleons on the last single-particle level we must consider the residual interaction and the calculations are more complex.

The experimental level scheme of $^{57}_{28}Ni$ is shown in Fig. 2.2. The ground state spin and parity $3/2^-$ corresponds to the $2p_{3/2}$ unpaired proton and also the first two levels are its successive excitations on the $1f_{5/2}$ and $2p_{1/2}$ single-particle levels. The next excited states cannot be explained in the same manner because we considered an inert core. In reality the core can have a collective excitations that will couple with the successive or simultaneous single particle excitations.

A similar approach can be applied for nuclei missing a nucleon in order to have a full shell. From a quantum physics point-of-view, the missing nucleon can be seen as a "hole" or an "anti-nucleon" having the same spin and parity but negative charge. Its successive excitations are on the lower levels till it is energetically favorable for

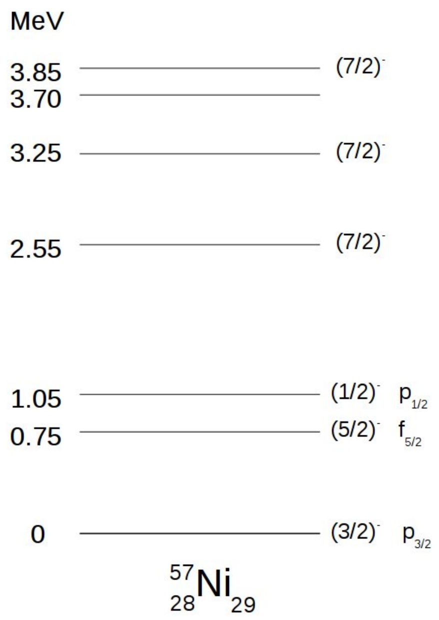

Figure 2.2: Level scheme of the first excited states in $^{57}_{28}$Ni.

a nucleon to "jump" in the next shell.

Odd-odd nuclei

The ground state configuration will be dictated by both the unpaired proton (n_p, l_p, j_p) and neutron (n_n, l_n, j_n). For most nuclei (n_p, l_p, j_p) will be different from (n_n, l_n, j_n) because neutron levels will be filled in advance of the proton levels. The parity will be given by the product $(-1)^{l_p}(-1)^{l_n}$ and the spin will take any integer value in the range:

$$|j_n - j_p| \leq I \leq j_n + j_p$$

By considering the residual interaction we can find out which spin corresponds for the ground state. To avoid this calculation, Nordheim proposed a semi-empirical rule based on the spin alignment of the proton and neutron in the deuteron for which the spin and parity is experimentally measured as $I^\pi = 1^+$. This corresponds to parallel orientation of the two nucleons. The Nordheim rule states that:

a) If $\quad j_p = l_p \pm 1/2 \quad$ and $\quad j_n = l_n \mp 1/2$

the ground state spin is $\quad I = |j_n - j_p|$

a) If $\quad j_p = l_p \pm 1/2 \quad$ and $\quad j_n = l_n \pm 1/2$

the ground state spin is $I = j_n + j_p$

The excited states will be defined by the vectorial coupling between the excited odd proton and neutron. Similar to the ground state, the single-particle shell model cannot establish the ordering and the spins and parities for the excited states. Only by considering the residual interaction we can obtain this information.

2.2 Properties of gamma decay

2.2.1 Energy conservation

Gamma radiation is usually emitted by nuclei in excited states which decay to a lower energy state or to the ground state. This decay can be direct or through a cascade of several transitions. The energy difference between the initial and final state is transformed into electromagnetic radiation having energies in the range of few keV (kilo electron-volts) to several MeV. The decay mechanisms of an excited nuclear state are only dependent of the characteristics of the initial and final states and are not influenced by the mechanism through which the initial state was populated.

If the energy difference between the initial and final levels is higher than the separation energy of a particle (alpha or nucleon) then gamma decay is less probable than the particle emission mechanism. These high energy states can only be achieved through nuclear reactions. If particle emission is energetically forbidden, the only decay mechanism is through electromagnetic gamma radiation. If the gamma energy is higher than $2m_ec^2 = 1.022$ MeV, gamma radiation will be in competition with electron-positron pair generation. If the energy difference is of the order of a few keV or tens of keV, the main decay mechanism is electron conversion. This mechanism will be covered in a future section.

According to Fig. 2.3 and considering the nucleus initially at rest, the following energy and momentum conservation laws apply:

$$\begin{aligned} m_ic^2 &= m_fc^2 + T_N + E_\gamma \\ \vec{0} &= \vec{p_N} + \vec{p_\gamma} \end{aligned}$$

Gamma radiations are photons without mass and have total energy $E_\gamma = \hbar\omega$ and momentum $p_\gamma = \frac{\hbar\omega}{c}$. The recoil energy of the nucleus $T_N = \frac{p_N^2}{2m_f} = \frac{p_\gamma^2}{2m_f} = \frac{E_\gamma^2}{2m_fc^2}$

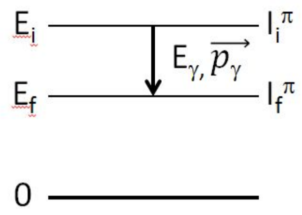

Figure 2.3: Simple nuclear level scheme showing a transition between two excited levels and the corresponding notations. The ground state is considered to have excitation energy zero.

is of the order of a few eV and is negligible in most cases except when considering the Mössbauer effect.

Considering the mass of the nucleus in the ground state m_0c^2 we can define the excitation energies of the two excited states as:

$$E_i = m_0c^2 + m_ic^2$$
$$E_f = m_0c^2 + m_fc^2$$

2.2.2 Spin and parity conservation

We define the gamma ray multipole L as the total angular momentum transferred by the gamma transition. Considering the spin and parity of the initial and final levels I_i^π and I_f^π, we have the following spin and parity conservation rules:

$$\vec{I_i} = \vec{I_f} + \vec{L}$$
$$\pi_i = \pi_f\pi_\gamma$$

For particles with mass, the total angular momentum is defined as the sum of the angular momentum and the intrinsic spin. In the case of photons, which are massless particles, we define the spin as the minimum value of the total angular momentum. Experimental evidence has shown that the photon spin is $\vec{S_\gamma} = 1$.

$$\vec{L} = \vec{l_\gamma} + \vec{1}$$

The transferred angular momentum can take any integer value greater than 1 according to the relation:

$$|I_i - I_f| \leq L \leq I_i + I_f; \quad L \geq 1$$

The parity of the gamma transition establishes its electric (E) or magnetic (M) character

$$\pi_\gamma = \pi_i \pi_f = \begin{cases} (-1)^L & \text{EL transition} \\ (-1)^{L+1} & \text{ML transition} \end{cases}$$

We get the following gamma multipolarities depending of the initial and final parity of the nuclear states:

$$\begin{aligned} M1 + E2 + M3 + E4 + ... \quad & \text{for} \quad \pi_\gamma = +1 \\ E1 + M2 + E3 + M4 + ... \quad & \text{for} \quad \pi_\gamma = -1 \end{aligned}$$

For example, considering both spin and parity conservation for the states $I_i^\pi = 5/2^-$, $I_f^\pi = 3/2^+$ we obtain the following possible gamma multipolarities:

$$\begin{aligned} (5/2 - 3/2) \leq & L \leq (5/2 + 3/2) \Rightarrow L = 1, 2, 3, 4 \\ & \pi_\gamma = (-1)(+1) = -1 \\ & \quad \Rightarrow E1, M2, E3, M4 \end{aligned}$$

The result is a mixing of several multiploarities with different transition probabilities. If one of the states has spin zero, the resulting transitions is a pure electric or magnetic transition. If both states have spin zero, gamma decay is forbidden because the resulting photons will have total angular momentum zero.

2.2.3 Transition probabilities

Experimental evidence has shown that the transition probability is rapidly decreasing for higher multipoles and, for the same multipole, the electric type is more probable than the magnetic one. Let us consider $L_m = |\vec{I_i} - \vec{I_f}|$ the smallest value of the gamma multipole between two states. We can observe experimentally the mixing $ML_m + E(L_m+1)$ in comparable ratios (mixing ratios) or $EL_m + M(L_m+1)$ where the electric transition is several orders of magnitude more probable than the magnetic transition. For single particle level transitions, the transition probabilities λ_γ have the following formulas:

$$\lambda_\gamma(XL) = \frac{1}{4\pi\varepsilon_0}\frac{8\pi}{((2L+1)!!)^2}\frac{L+1}{\hbar L}\left(\frac{\omega}{c}\right)^{2L+1}B(XL)_\downarrow$$

Where B(XL) are electric (EL) or magnetic (ML) nuclear matrix elements that describe the transition between the initial and final state. They may be calculated with a theoretical model for comparison with experiment.

$$B(XL)_\downarrow = \sum_M \left[\int \Psi_f^\star O_M(XL)\Psi_i d\vec{r}\right]^2$$

Here, $\Psi_i(\vec{r})$ and $\Psi_f(\vec{r})$ are wavefunctions for the single particle states and we sum all the possible values of the angular momentum projection M. $O(XL)$ is the magnetic or electric transition operator. Weisskopf derived the the following single particle estimates for these matrix elements based on the shell model:

$$B_{SP}(EL) = \frac{R^{2L}}{4\pi b^L}\left(\frac{3}{3+L}\right)^2$$
$$B_{SP}(ML) = \frac{R^{2L-2}}{\pi b^{L-1}}\left(\frac{3}{3+L}\right)^2$$

Where $b = 10^{-24}\ cm^2$ and $R = 1.2 \cdot 10^{-13}A^{1/3}\ cm$. A simple observation is that the gamma transition probability is proportional with the energy and is lower if the transferred angular momentum is higher. The various multipoles plotted in Fig. 2.4 separate relatively well except for $E1$ and $E2$ that have similar lifetimes. The increased strength of the $E2$ transitions is due to collective quadrupole motions of several nucleons and $E1$ transitions are usually viewed as single nucleon transitions. The single particle transition half-life can be calculated based on the Weisskopf estimates:

$$T_{1/2}(XL)_{SP} = \frac{ln(2)}{\lambda_\gamma(XL)}$$

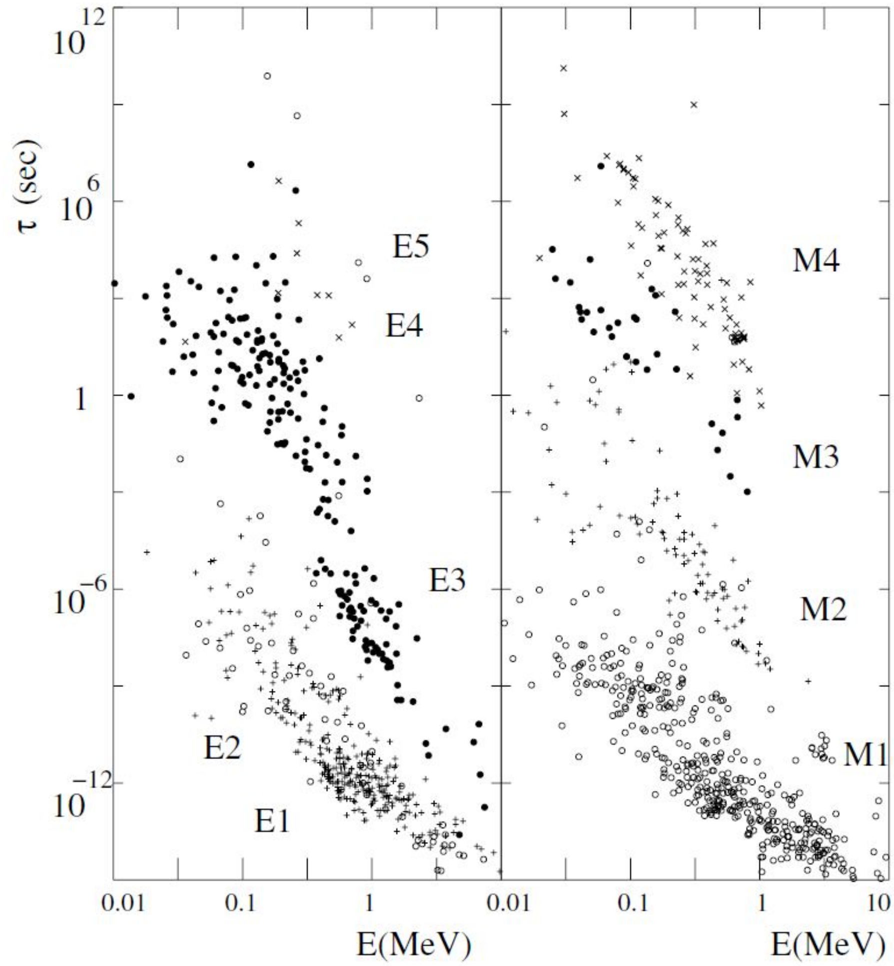

Figure 2.4: Experimental transition lifetimes as a function of E_γ. Figure taken from [9].

It is usually observed experimentally the mixing between M1 and E2 due to similar orders of magnitude. The mixing ratio is simply defined as:

$$\delta^2_{E2/M1} = \frac{\lambda(E2; J_i^\pi \to J_f^\pi)}{\lambda(M1; J_i^\pi \to J_f^\pi)}$$

Table 1. Formulae for single-particle transition half-lives, corrected for internal conversion.

Electric	$t_{1/2}^{\gamma}$ (s)	Magnetic	$t_{1/2}^{\gamma}$ (s)
E1	$\frac{6.76\times10^{-6}}{E_\gamma^3 A^{2/3}}$	M1	$\frac{2.20\times10^{-5}}{E_\gamma^3}$
E2	$\frac{9.52\times10^{6}}{E_\gamma^5 A^{4/3}}$	M2	$\frac{3.10\times10^{7}}{E_\gamma^5 A^{2/3}}$
E3	$\frac{2.04\times10^{19}}{E_\gamma^7 A^{2}}$	M3	$\frac{6.66\times10^{19}}{E_\gamma^7 A^{4/3}}$
E4	$\frac{6.50\times10^{31}}{E_\gamma^9 A^{8/3}}$	M4	$\frac{2.12\times10^{32}}{E_\gamma^9 A^{2}}$
E5	$\frac{2.89\times10^{44}}{E_\gamma^{11} A^{10/3}}$	M5	$\frac{9.42\times10^{44}}{E_\gamma^{11} A^{8/3}}$

Table 2. $t_{1/2}$(W.u.)/$t_{1/2}$(exp) (Recommended Upper Limits)

Multipolarity	5≤A≤44[a]	45≤A≤90	91≤A≤150	A≥151
E1 (isovector)	0.5[b]	0.01	0.01	0.01
E2 (isoscalar)	100	300	300	1000
E3	50	100	100	100
E4	50	100	30	
M1 (isovector)	10[c]	3	3	2
M2 (isovector)	5	1	1	1
M3 (isovector)	10	10	10	10
M4		30	30	10

[a] 0.002 for E1 (isoscalar), 5 for E2 (isovector), 0.05 for M1 (isoscalar), and 0.2 for M2 (isoscalar).
[b] 0.1 for 21≤A≤44
[c] 5 for 21≤A≤44

In Table 1, taken from [12], are represented some simple equations for single-particle half-lives of $L = 1 - 5$ order transitions. Systematics for the ratio of the single-particle half-life to the experimental half-life can be used to help restrict the range of possible transition multipolarities. In Table 2 are shown the recommended upper limits derived by P.M. Endt [13] for A<150. These limits apply with a good agreement for spherical nuclei. In deformed nuclei, $E2$ transitions are collectively enhanced such that the experimental half-life is even smaller and the recommended upper limits should be raised by an order-of-magnitude.

2.2.4 Branching ratio

A nuclear level can de-excite through several transitions. The total transition probability of the level which is measured experimentally is the sum of individual transition probabilities for each decay channel including internal conversion:

$$\lambda_T = \frac{1}{\tau} = \sum \lambda_i^{\gamma} + \sum \lambda_i^{IC}$$

The partial transition probabilities can be deduced from the intensity of each decay channel. The branching ratio is proportional with the transition probability and measured experimentally as the intensity ratio between each decay channel and the most intense transition normalised as 100.

$$b_{1,2} = \frac{I_1}{I_2} = \frac{\lambda_1}{\lambda_2}$$

The only method that can be used in order to measure partial transition lifetimes is possible only for levels which decay both by gamma transitions and internal conversion. By stripping all the electrons from the atomic electron shell, the internal conversion mechanism is blocked and the measured lifetime is higher than in the full electron shell case.

2.2.5 Internal conversion

Internal conversion represents the process through which an excited nucleus directly transfers it's excitation energy to an atomic inner shell electron. The electron will have kinetic energy T_e equal with the difference between the total transition energy E_0 and the electron binding energy for the corresponding shell j:

$$T_e = E_0 - B_j; \quad j = K, L, M, ...$$

The resulting electrons from shells K, L, M, ... , will be mono-energetic, their spectra being the discreet lines overlapping with the continuous spectra of the beta electrons as it is shown in Fig. 2.6. The hole left in the electron shell by the ejected conversion electron will be filled by another atomic electron. This transition will produce characteristic X-rays and Auger electrons. The production mechanism of the Auger can be understood as an atomic analogy of the nuclear process of internal conversion.

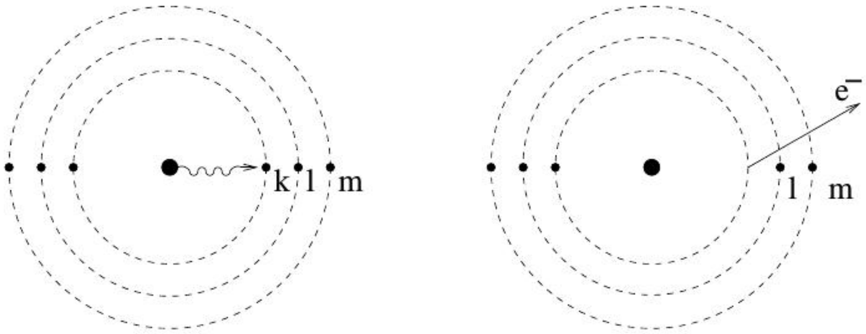

Figure 2.5: Schematic representation of the internal conversion mechanism. Note that the undulated line represents the electromagnetic interaction between the nuclear field and the electron and should not be considered a gamma radiation. Figure taken from [9].

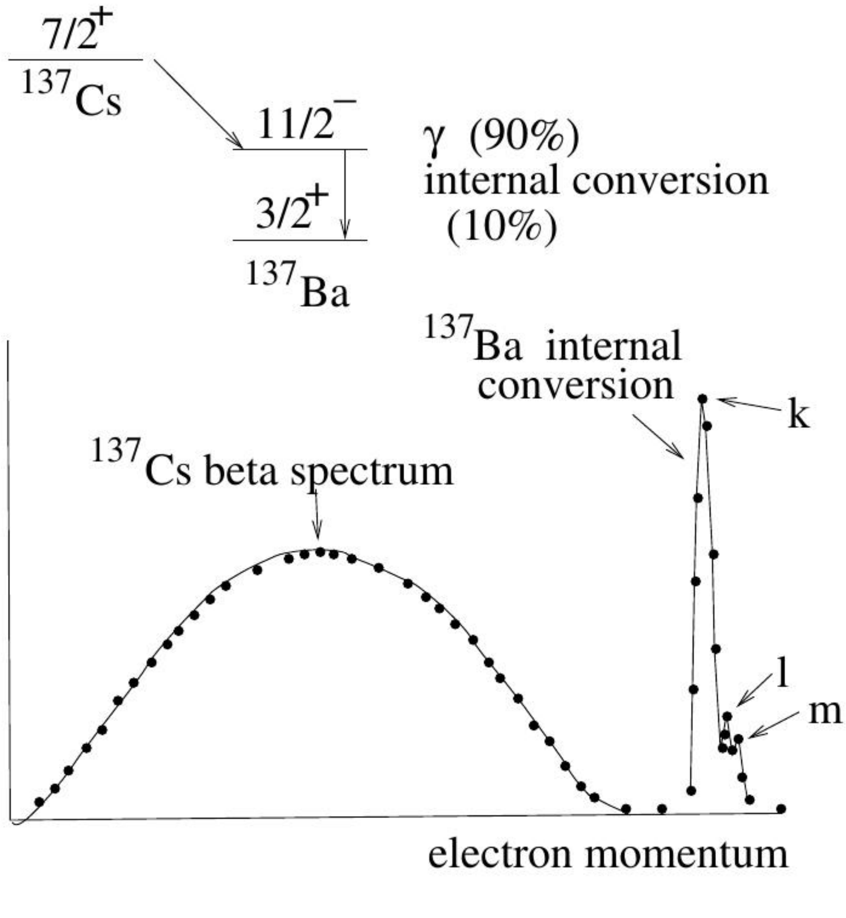

Figure 2.6: Beta-decay spectrum of ^{137}Cs and internal conversion lines from the radiative decay of the first excited state of ^{137}Ba. Figure taken from [9].

The internal conversion mechanism is a single step process and not a two step process in which a gamma ray produced by the excited nucleus will transfer it's energy to an atomic electron. This is supported by the following experimental evidence:

1. Conversion electrons appear even in gamma forbidden $L = 0(0 \rightarrow 0)$ transitions

2. The internal conversion probability is higher when the energy difference between the initial and final states is lower and the spin difference is higher. This is the opposite compared to the gamma transition probability.

The competition between the two decay processes can be described by the internal conversion coefficient α:

$$\alpha = \frac{\lambda_e}{\lambda_\gamma} = \frac{I_e}{I_\gamma}$$

where λ is the decay probability, proportional with the intensity of the corresponding decay process.

We can also define the internal conversion coefficient as a sum of partial conversion coefficients for each atomic shell:

$$\alpha = \frac{\lambda_K + \lambda_L + ...}{\lambda_\gamma} = \alpha_K + \alpha_L + ...$$

Due to the fact that the K shell is closer to the nucleus, α_K is higher than α_L and so on. From the simple beta decay scheme shown in Fig. 2.6 we can estimate the partial internal conversion coefficients by measuring the area A_i corresponding to each shell and normalising to the total number of beta electrons:

$$\alpha_i = \frac{A_i}{A_\beta - (A_K + A_L + ...)}; \quad i = K, L, M, ...$$

The experimental evidence is confirmed by theoretical calculations, evidencing the same dependency of the internal conversion coefficient with the electric or magnetic transition multipole L, gamma energy E_γ, atomic number Z and principal quantum number n_x for the K, L, M atomic shells.

$$\alpha_x(EL) = Z^3 \left(\frac{2m_e c^2}{E_\gamma}\right)^{L+5/2} \frac{1}{n_x^3}$$
$$\alpha_x(ML) = Z^3 \left(\frac{2m_e c^2}{E_\gamma}\right)^{L+3/2} \frac{1}{n_x^3}$$

The total decay probability for a nuclear level must take into account the internal conversion coefficient:

$$\lambda = \lambda_\gamma + \lambda_e = \lambda_\gamma(1+\alpha)$$
$$\tau = \frac{1}{\lambda} = \frac{1}{\lambda_\gamma(1+\alpha)} = \frac{\tau_\gamma}{1+\alpha}$$

2.3 Properties of beta decay

Beta decay can occur in three possible ways which must involve another charged particle to conserve electric charge. The charged particle, originally called a β particle, was later shown to be the electron.

$$\mathrm{n} \rightarrow \mathrm{p} + \mathrm{e}^- + \bar{\nu} \qquad \beta^- \text{ decay}$$
$$\mathrm{p} \rightarrow \mathrm{n} + \mathrm{e}^+ + \nu \qquad \beta^+ \text{ decay}$$
$$\mathrm{p} + \mathrm{e}^- \rightarrow \mathrm{n} + \nu \qquad \text{electron capture } (\varepsilon)$$

The first process is known as negative β decay and involves the creation and emission of an ordinary electron. The second process is positive β decay or positron decay, in which a positively charged electron is emitted. In the third process, an atomic electron that strays too close to the nucleus is swallowed, allowing the conversion of a proton to a neutron. The latter two processes occur only for protons bound in nuclei, being energetically forbidden for free protons or for protons in hydrogen atoms.

In all three processes, another particle called a *neutrino* is also emitted, but since the neutrino has no electric charge, its inclusion in the decay process does not affect the identity of the other final particles. In a nucleus, β decay changes both Z and N by one unit: $Z \rightarrow Z \pm 1$, $N \rightarrow N \mp 1$ so that $A = Z + N$ remains constant.

We define the Q_β value to be the difference between the initial and final nuclear mass energies. This released energy is shared between the electron and the neutrino.

The maximum energy of the electron E_{max} is approximately Q_β provided that the neutrino has zero energy. Let us cosider a typical negative beta decay process in a nucleus:

$$
{}^A_Z X_N \rightarrow {}^A_{Z+1} X'_{N-1} + e^- + \bar{\nu}
$$
$$
Q_\beta = \left(m_{{}^A_Z X} - m_{{}^A_{Z+1} X'} - m_e \right) c^2
$$

The above expression represents a decay between two nuclear ground states. If the populated state in the daughter nucleus is an excited state, the Q value must be decreased by the excitation energy of the populated state:

$$
Q_\beta^{ex} = Q_\beta^{gs} - E_{ex}
$$

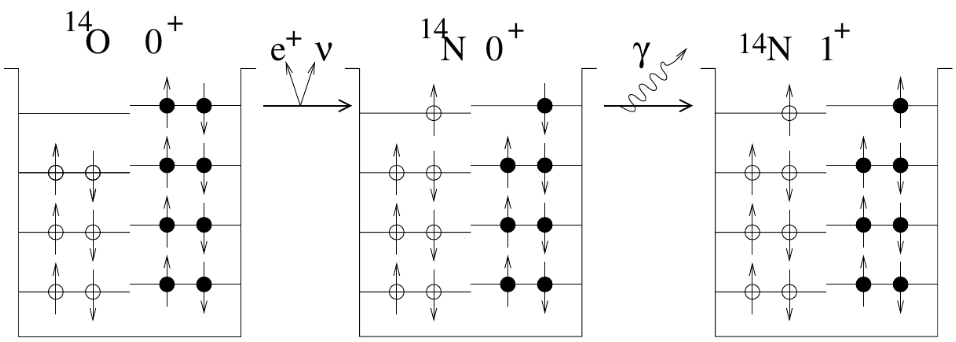

Figure 2.7: Schematic representation of the beta decay of ${}^{14}O$. This decay is predominantly to the first excited state (0^+) in ${}^{14}N$ followed by a radiative decay to the ground state (1^+). There are two valence protons, both of which can decay into a neutron. Figure taken from [9].

2.3.1 Decay lifetimes and log*ft* values

The transition probability of a beta emitter can be derived using the first-order time dependent perturbation theory. The transition mean lifetime τ is expressed in terms of the squared matrix element describing the initial and final states and a statistical factor which indicates how the energy is distributed among the beta particles.

$$\lambda_\beta = \frac{1}{\tau} = G^2|M|^2 \int_1^{E_{max}} F(Z, E_e)(E_{max} - E_e)^2 E_e p_e dE_e$$

where p_e is the momentum and E_{max} is the maximum energy E_e of the beta particles. G^2 is the Fermi coupling constant. The $F(Z, E_e)$ function varies slowly at small values of Z but more rapidly after $Z = 20$. The value of the integral can be represented as a function $f(Z, E_{max})$:

$$\frac{1}{\tau} = G^2|M|^2 f(Z, E_{max}) \quad \rightarrow \quad f\tau = \frac{1}{G^2|M|^2}$$

In practice we use the logarithm of $f\tau$ or ft value which depends on the atomic number Z, the end point energy Q_β (or E_{max}) and the mean life τ or half-life $T_{1/2} = 0.693{\cdot}\tau$. The allowed or forbidden nature of the beta transition is determined by the ft value. Higher values are related to a large spin change in the transition which are usually forbidden. Thus we can describe beta transitions in terms of the logft systematics as shown in Fig. 2.8.

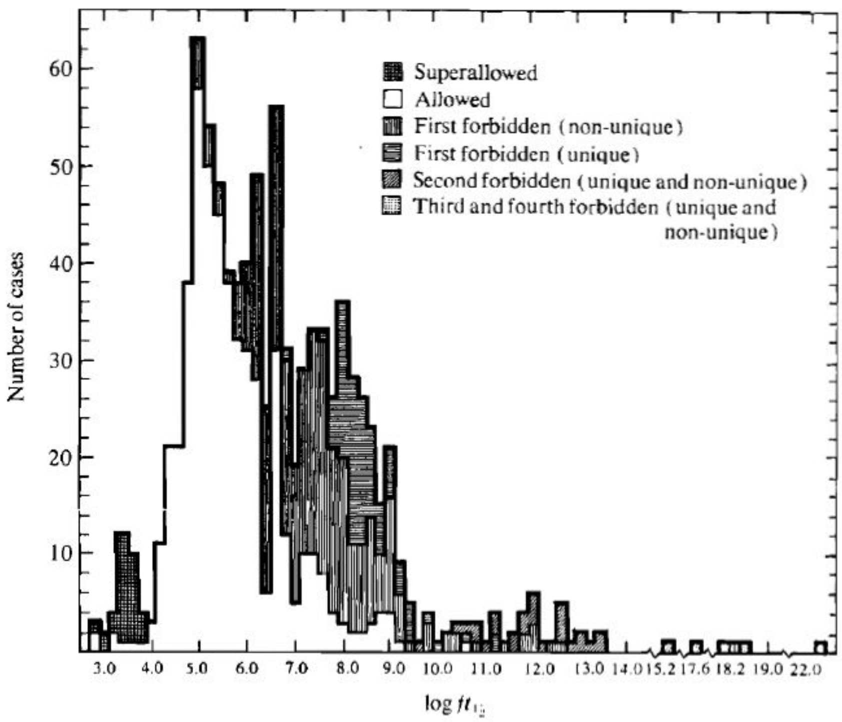

Figure 2.8: Distribution of known logft values for various beta emitters. Figure taken from [14].

2.3.2 Selection rules for beta decay

The two resulting leptons, electron/positron and antineutrino/neutrino can be emitted in a singlet state (spins antiparallel) or in a triplet state (spins parallel). The Fermi selection rule requires that the neutrinos and electrons to be emitted in a singlet state, thus $\delta j = 0$ ($j_i = j_f$). In the triplet state $j_f = j_i$ or $j_f = j_i \pm 1$, which are Gamow-Teller transitions. One exception is the $0^+ \rightarrow 0^+$ transition which is forbidden according to the Gamow-Teller selection rule. This represents a pure Fermi transition and it is shown in Fig. 2.7. The beta decay selection rules can be summarized as follows

$$\begin{aligned} \Delta j = 0; \quad & \Delta P = 0 \rightarrow \text{Fermi rule} \\ \Delta j = \pm 1, 0; \quad & \Delta P = 0 \rightarrow \text{Gamow-Teller rule} \quad (j_i = 0 \rightarrow j_f = 0 \text{ is forbidden}) \end{aligned}$$

Chapter 3

Gamma spectroscopy of ^{80}Ga following the β-decay of ^{80}Zn

3.1 Scientific motivation

The recent availability of clean, intense beams of radioactive isotopes close to the presumed doubly magic nucleus ^{78}Ni has triggered renewed interest in this region. The nucleus ^{78}Ni is doubly magic in the $\vec{l}.\vec{s}$ coupling scheme, though its suitability for use as a closed core in shell-model calculations remains uncertain. As it is the most neutron-rich doubly magic region currently accessible for experimental studies, then comparisons between spectroscopic data on the nuclei here and state-of-the-art shell-model calculations play a key role assessing the impact of neutron excess on effective nucleon-nucleon interactions. Spectroscopic information also allows the evolution of single-particle orbit energies to be followed, as a function of Z and N. In the present work γ decays of the three-valence-proton, one-valence-hole nucleus ^{80}Ga have been observed and compared to the predictions of shell-model calculations, allowing a sensitive test of neutron-proton interactions in this region.

Nuclear structure is an important input into rapid neutron-capture-process (r-process) nucleosynthesis calculations. The key parameters of interest are ground- and isomeric-state half-lives, and delayed-neutron emission probabilities, which are all influenced by shell structure. Any erosion of the $Z = 28$ and $N = 50$ shell closures would have an obvious impact on the direction and speed of the r-process reaction around the $A \sim 80$ abundance peak. Possible experimental evidence for the less-than-robust nature of the these shells includes mass measurements, which indicate that ^{78}Ni is not the most tightly bound nucleus of this region [15]. Recent shell-model calculations require the inclusion of orbits from below the $Z = 28$ shell closure in the valence space to correctly reproduce measured magnetic moments in the Cu isotopes [16].

A recent collinear laser-spectroscopy experiment has identified a 6^- isomeric state in ^{80}Ga, with a half-life > 200 ms [17], lying at an unknown energy above the 3^- ground state. Half-lives for the two β-decaying states were recently reported as

1.9-s and 1.3-s, although the spin and parity could not be established [18].

3.2 The ISOLDE facility and the IS441 experimental setup

The on-line isotope mass separator ISOLDE [19] is a facility dedicated to the production of a large variety of radioactive ion beams for many different experiments in the fields of nuclear and atomic physics, solid-state physics, materials science and life sciences. ISOLDE, an acronym for Isotope Separator On Line DEvice, was originally proposed at the 600 MeV Proton Synchrocyclotron in 1964 at CERN, the European Organization for Nuclear Research. The first experiments started there in 1967. ISOLDE underwent several upgrades until it was finally moved to the PSB in 1992. It is operated by the ISOLDE collaboration, whose present members are Belgium, CERN, Denmark, Finland, France, Germany, Greece, India, Ireland, Italy, Norway, Romania, Spain, Sweden and the United Kingdom.

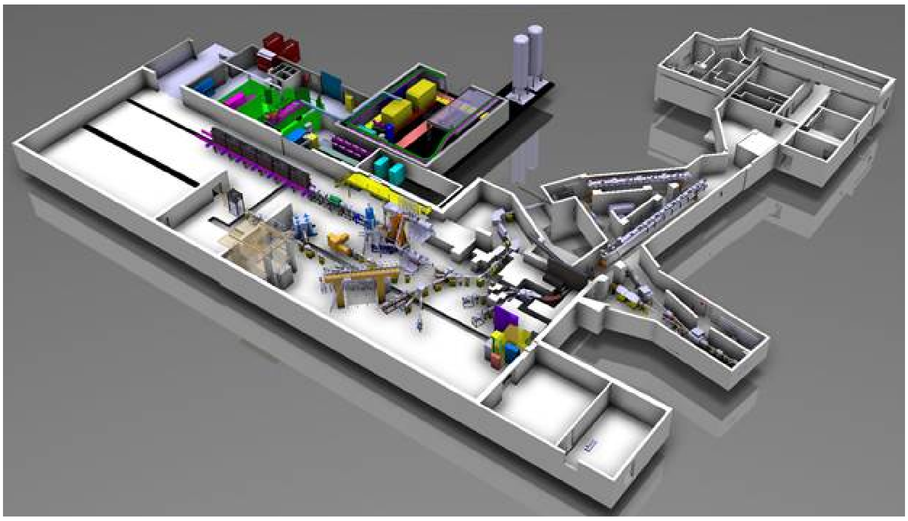

Figure 3.1: 3D layout of ISOLDE. Figure taken from http://isolde.web.cern.ch/

The facility has been in operation since its start in 1967 and is presently receiving protons from the Proton Synchrotron Booster (PSB) of CERN. The success of ISOLDE is due to the continuous development of new radioactive ion beams and improvement of the experimental conditions. With the upcoming high energy and intensity upgrade HIE-ISOLDE, the possibilities for experiments with exotic nuclei will be further boosted.

The β^- decay spectroscopy of ^{80}Zn was performed at ISOLDE as part of systematic ultra-fast timing studies of neutron rich Zn nuclei. Two similar experiments have been performed but using slightly different production means of ^{80}Zn. In the first experiment (2009), the ^{80}Zn nuclides were produced by the CERN PS Booster 1.4-GeV proton-beam impinging directly on the thick uranium carbide target shown in Fig. 3.2. This production mechanism was responsible for a strong production of proton-rich impurities at mass 80. In the second experiment (2011) the PS Booster proton-beam was directed to a neutron converter which fast neutron beam induced fission in the uranium carbide target. The reaction products diffused from the 2000 $^{\circ}C$ hot target via a quartz chemically selective transfer line into a tungsten ionizer where resonant laser ionization was used to produced an intense and pure Zn ion beam [20, 21, 22].

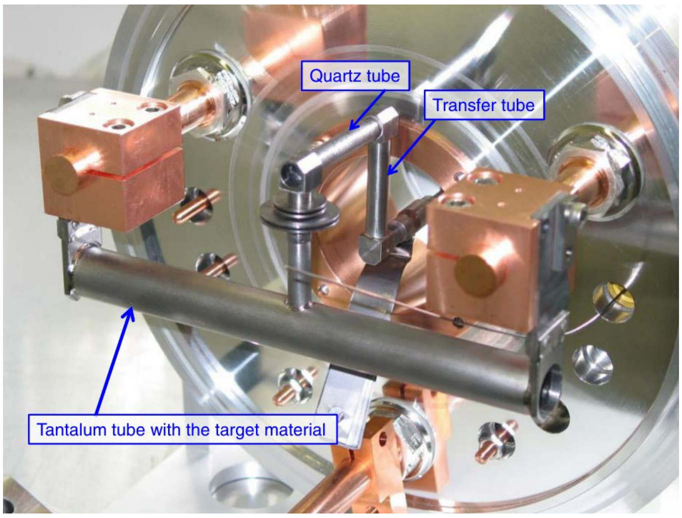

Figure 3.2: Photo of the ISOLDE target unit. The heated tantalum container containing UCx (uranium carbide) is connected to the ion source via a quartz controlled transfer tube which absorbs the rubidium atoms. Figure taken from [23].

After extraction and acceleration to 40 keV, the ISOLDE high-resolution separator was used to mass select an $A = 80$ beam. Around 20000 ions/s, were sent to an aluminium catcher foil at the center of the array of β and γ detectors shown in Fig. 3.4.

The detection system consisted of a 3-mm thick NE111 plastic scintillator positioned less than 0.5 mm behind an Al foil at the ion collection point. This detector was used as a fast-response β-detector. The thickness of the plastic scintillator was chosen to yield an almost uniform time response to β particles within a wide range of energies. Two conical, 1.5-in long $LaBr_3(Ce)$ crystals were used as fast-response γ detectors. In addition, two HPGe detectors were present, with relative efficien-

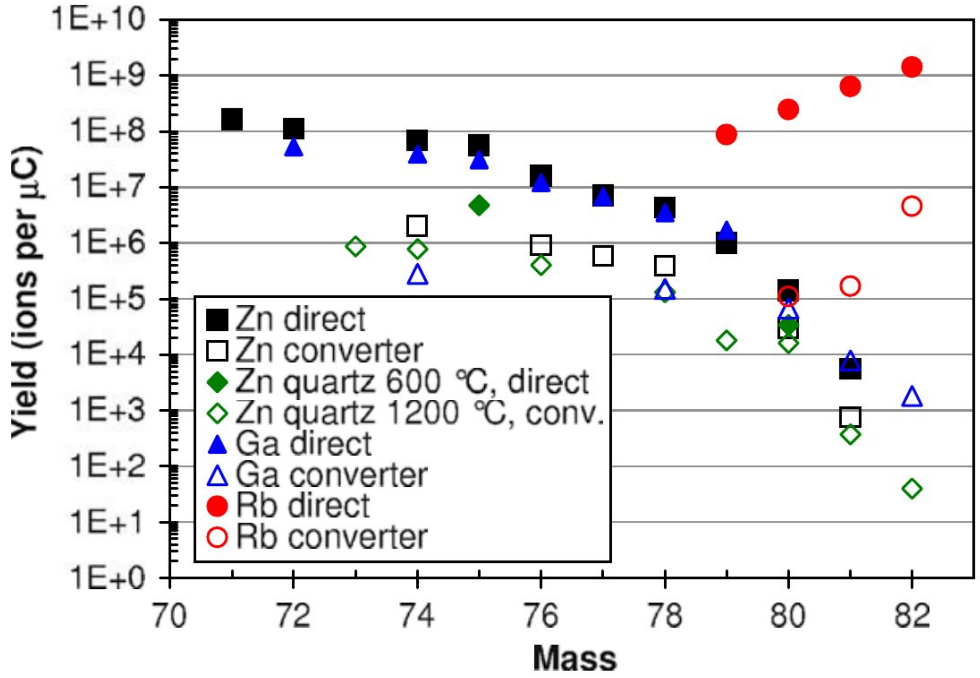

Figure 3.3: ISOLDE yields of Zn, Ga and Rb isotopes showing the difference between sending 1.4 GeV protons directly to the UCx target and sending them indirectly onto a tungsten converter mounted parallel to the target. For mass $A = 80$, Rb contamination is reduced with three orders of magnitude. Figure taken from [22].

cies of about 60 %, covering an energy range of 30 to 4000 keV. These were used to provide a unique selection of γ-decay branches in $\beta - \gamma(E) - \gamma(t)$ fast-timing measurements [24, 25] and to study $\gamma - \gamma$ coincidences, in order to determine the level scheme.

A 16-parameter PIXIE-4 digital data acquisition (DAQ) system [26] was used to collect energy signal from all 5 detectors, along with the time of arrival of the proton pulse on the target or convertor. Moreover, the DAQ system (Fig. 3.6) also collected 5 time-to-amplitude convertor (TAC) signals. Four of the TACs were started by the β signal and stopped by each of the γ detectors, whereas the fifth TAC was started by one $LaBr_3$(Ce) detector and stopped by the other. The TAC range for the fast-timing detectors was set to 50 ns, whereas the one stopped by Ge detectors had a range of 2 μs. The energy and efficiency calibrations of the γ detectors were determined using sources of ^{140,133}Ba, ^{138}Cs and ^{152}Eu. For the present analysis only the β and HPGe detector signals from the 2011 experiment and β–$LaBr_3$(Ce) coincidences from the 2009 experiment are used.

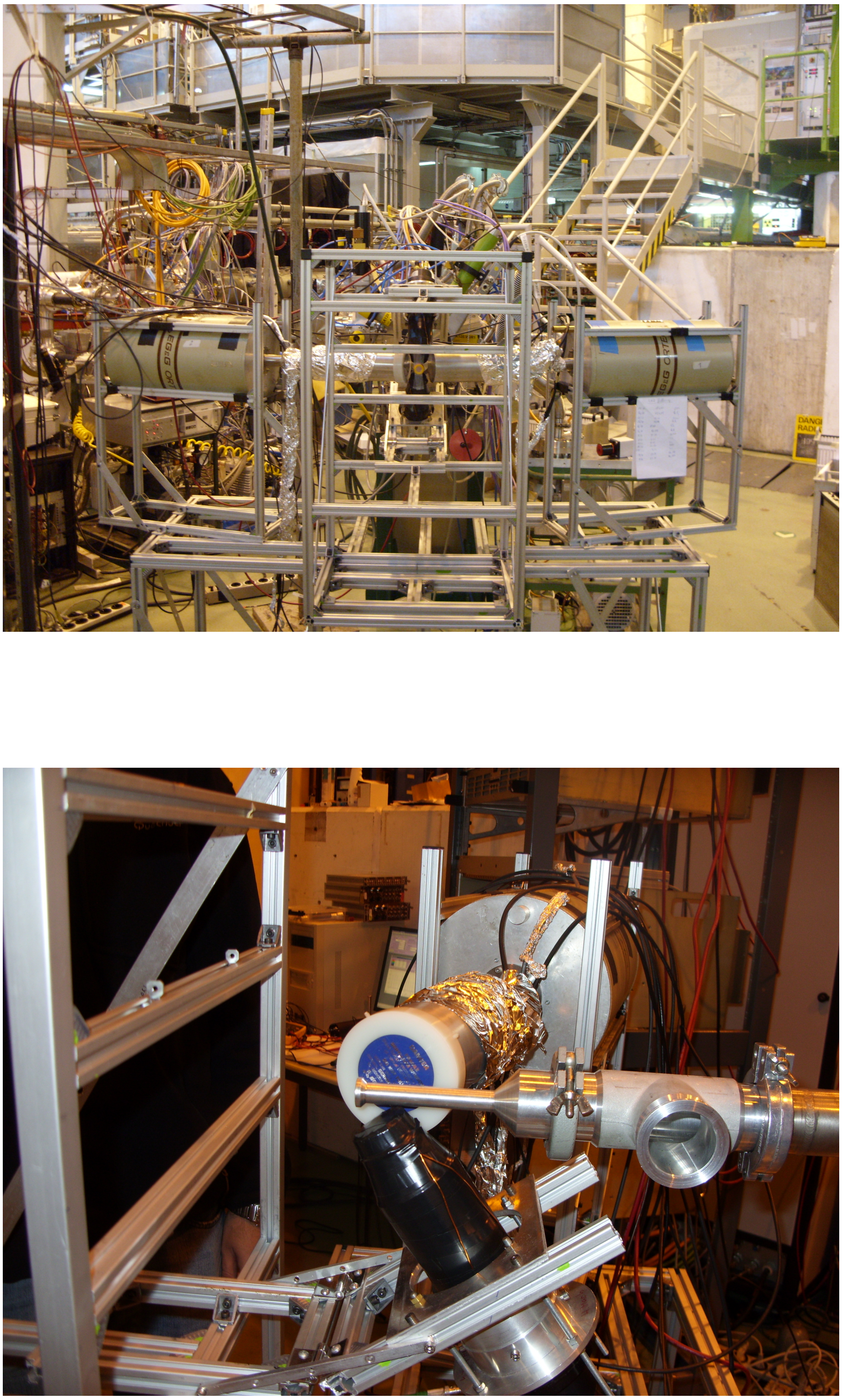

Figure 3.4: Photos of the IS441 detection array.

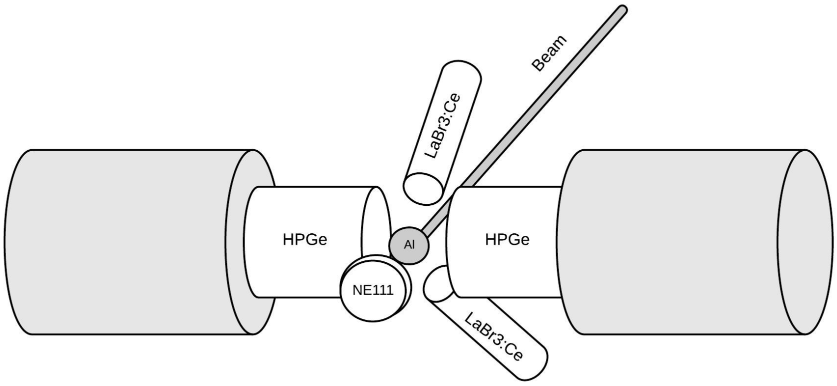

Figure 3.5: Schematic representation of the IS441 detection setup.

3.3 Experimental results

3.3.1 Improved level scheme. Absolute gamma intensities

Gamma ray transitions that belong to the decay of excited states in ^{80}Ga were assigned both by starting from previously known transitions, and by examining coincidence spectra. There are a total of 86 identified transitions listed in Table 3.1. The level scheme of ^{80}Ga, as determined in the present experiment, is in good agreement with the previous published results in [27] and [28]. This level scheme is shown in Fig. 3.8. Several new energy levels are postulated by strong coincidences between all of the previously reported γ rays and the newly discovered ones.

In Fig. 3 from [27], the placement of the 403 keV gamma ray was questionable because no coincidence with 282 and 614 keV was observed in the current coincidence spectra, as shown in Fig. 3.7. The 74, 174, 312, 403, 636 and 1116 keV gamma rays were repositioned in the new level scheme such that the 403 keV was directly feeding the new ground state which is 22.4 keV lower than the next excited level. The new ground state was found based on the fact that the above mentioned γ rays were coincident with 1151, 1034 and 566 keV transitions and that 403, 174, 636 and 312 keV γ rays were mutually coincident, as being part of a cascade. One of the possible configurations was the four transitions would succeed each other starting from the 1526 keV level. Their order was later confirmed by coincidences with additional newly discovered transitions.

The level scheme and results reported in [17] suggest that the ground state has spin and parity 6^- and would feed by beta decay the spin 8^+ from ^{80}Ge reported

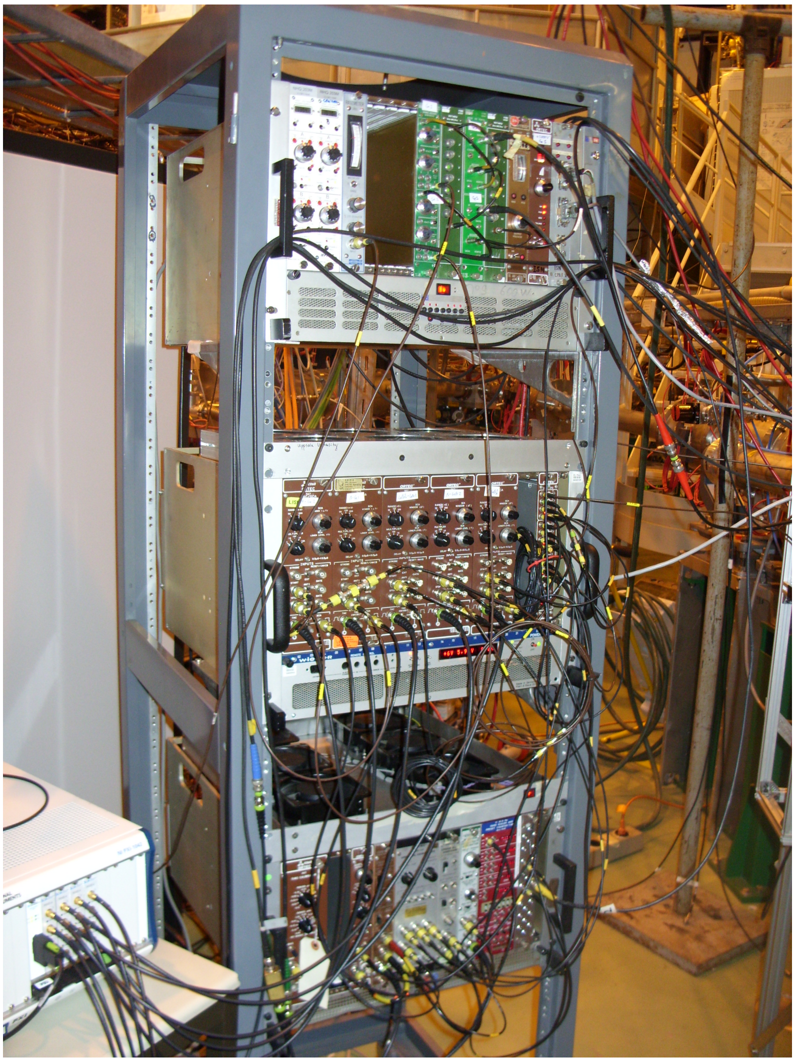

Figure 3.6: Photo of the IS441 detection electronics.

in [29]. The first excited state should then have spin and parity 3^- being the long lived isomer discovered by collinear laser spectroscopy in [17].

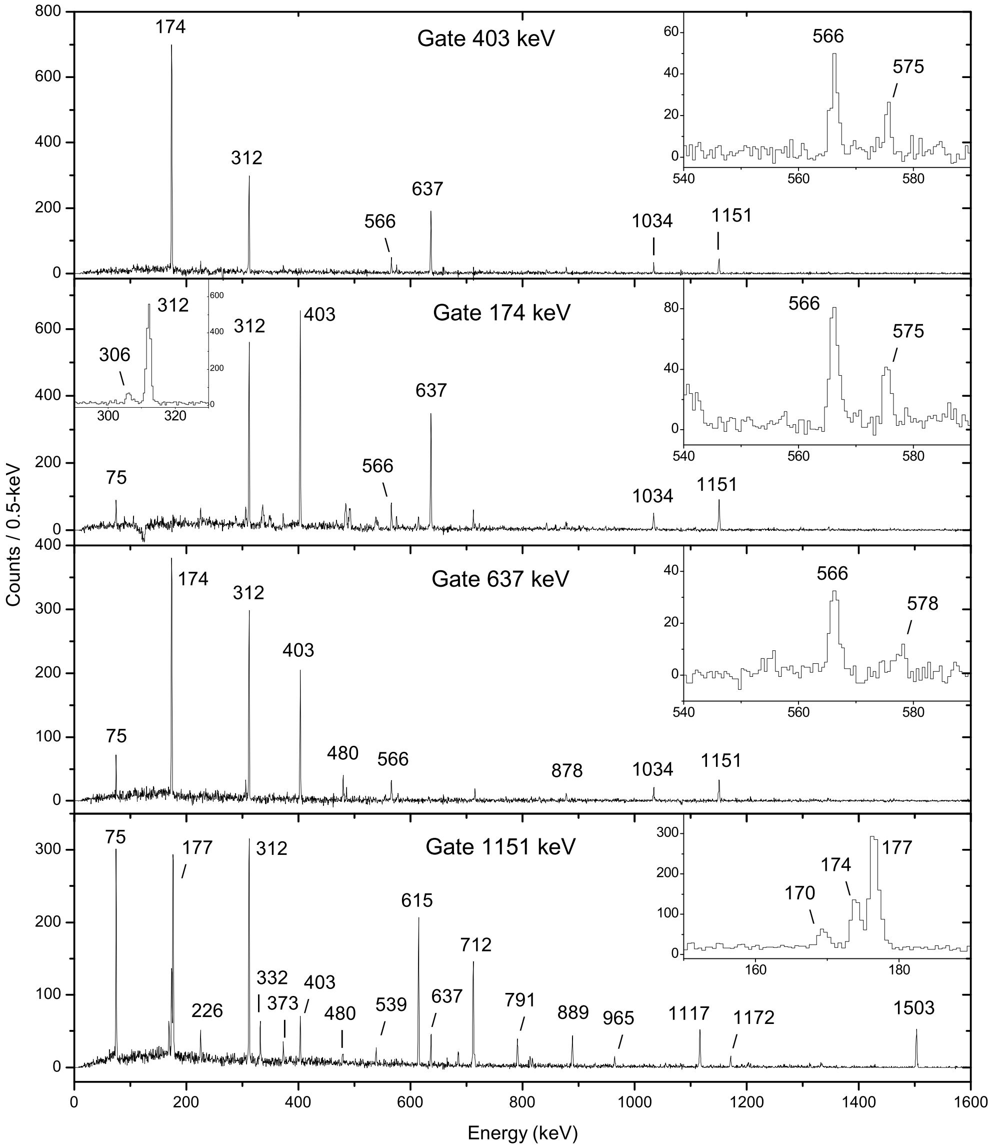

Figure 3.7: HPGe $\gamma-\gamma$ coincidence spectra containing transitions from ^{80}Ga with gates on the relevant 403-keV, 174-keV, 637-keV and 1151-keV transitions.

Table 3.1: Gamma-ray transitions in ^{80}Ga, as found in the present work, associated with the level scheme shown in Fig. 3.8. The transition intensities are normalized to that of the 712-keV gamma ray, taken as 100. For absolute intensity per 100 decays, multiply the relative intensity by 0.41(6). The tentative γ rays are marked with ^{t}. The strong transitions were calculated from the prompt γ singles spectrum and the weaker ones from coincidence spectra. All the errors are based on statistical uncertainties and fitting approximations.

E_γ (keV)	I_γ	Assignment $E_{initial}$	E_{final}	J_i^π	J_f^π
74.8(1)	10.8(2)	97.1	22.4	-	3^-
75.8(1)^t	<0.2	1526.0	1450.0	-	1^+
93.4(1)	3.2(6)	1450.0	1356.5	1^+	-
151.7(1)^t	<0.2	1141.9	990.0	-	-
154.7(1)	0.3(1)	1141.9	987.1	-	-
159.5(1)	1.2(3)	1450.0	1290.4	1^+	-
169.6(1)	1.4(3)	1526.0	1356.5	-	-
174.0(1)	5.6(6)	577.3	403.4	-	-
176.6(1)	10.1(10)	911.3	734.7	-	-
190.5(1)	2.3(2)	1141.9	951.4	-	-
203.6(1)	0.3(1)	1193.8	990.0	-	-
225.7(1)	1.2(2)	1526.0	1300.5	-	-
243.5(1)	0.9(2)	951.4	707.8	-	(1^+)
282.21(5)	4.1(4)	990.0	707.8	-	(1^+)
282.7(1)	0.6(2)	1193.8	911.3	-	-
306.4(1)	0.2(1)	403.4	97.1	-	-
308.3(1)	0.4(1)	1450.0	1141.9	1^+	-
312.13(5)	12.4(2)	1526.0	1213.9	-	-
332.17(5)	2.6(4)	1526.0	1193.8	-	-
373.2(1)	0.2(1)	1526.0	1152.7	-	-
403.47(3)	4.3(5)	403.4	0.0	-	6^-
406.9(2)	0.8(2)	1141.9	734.7	-	-
433.9(1)	2.2(4)	1141.9	707.8	-	(1^+)
444.9(1)	0.8(1)	1356.5	911.3	-	-
459.9(1)^t	<0.2	1450.0	990.0	1^+	-
462.72(2)	11.1(1)	1450.0	987.1	1^+	-
468.3(1)	2.2(6)	2560.4	2092.1	(1^+)	1^+
480.1(1)	0.7(1)	577.3	97.1	-	-

518.3(1)	1.0(2)	2044.5	1526.0	-	-
538.87(5)	1.3(2)	1526.0	987.1	-	-
566.20(5)	10(1)	2092.1	1526.0	1^+	-
575.3(1)	0.4(1)	1152.7	577.3	-	-
577.7(2)	0.2(1)	577.3	0.0	-	6^-
594.9(1)^t	0.3(1)	2044.5	1450.0	-	1^+
614.66(5)	13.3(4)	1526.0	911.3	-	-
621.8(1)	1.7(3)	1356.5	734.7	-	-
632.5(1)	3.5(4)	2677.0	2044.5	1^+	-
636.6(1)	4.5(5)	1213.9	577.3	-	-
642.3(1)	30(3)	2092.1	1450.0	1^+	1^+
685.4(1)	36(4)	707.8	22.4	(1^+)	3^-
688.0(1)	1.8(3)	2044.5	1356.5	-	-
712.3(1)	100(10)	734.7	22.4	-	3^-
723.2(8)^t	<0.2	1300.5	577.3	-	-
715.2(1)	77(21)	1450.0	734.7	1^+	-
735.6(1)	2.2(4)	2092.1	1356.5	1^+	-
742.0(1)	21(2)	1450.0	707.8	1^+	(1^+)
791.3(1)	4.0(6)	1526.0	734.7	-	-
802.0(1)	0.8(2)	2092.1	1290.4	1^+	-
814.2(1)	1.6(2)	911.3	97.1	-	-
818.2(1)	1.1(3)	1526.0	707.8	-	(1^+)
878.2(2)	1.0(2)	2092.1	1213.9	1^+	-
888.9(1)	5.7(6)	911.3	22.4	-	3^-
928.8(2)	13.6(15)	951.4	22.4	-	3^-
950.5(2)	1.3(3)	2092.1	1141.9	1^+	-
964.8(2)	32(3)	987.1	22.4	-	3^-
1034.3(2)	9.2(10)	2560.4	1526.0	(1^+)	-
1057.3(3)	0.6(2)	2044.5	987.1	-	-
1104.9(2)	5.4(7)	2092.1	987.1	1^+	-
1110.3(2)	1.8(6)	2560.4	1450.0	(1^+)	1^+
1116.7(2)	9.0(10)	1213.9	97.1	-	-
1150.9(2)	22(2)	2677.0	1526.0	1^+	-
1171.5(2)	3.9(5)	1193.8	22.4	-	3^-
1203.3(2)	1.1(2)	1300.5	97.1	-	-
1226.9(2)	3.2(8)	2677.0	1450.0	1^+	1^+
1267.9(2)	5.9(7)	1290.4	22.4	-	3^-
1296.2(2)	1.7(6)	2822.1	1526.0	-	-
1320.6(2)	2.0(5)	2677.0	1356.5	1^+	-
1334.0(2)	9.9(11)	1356.5	22.4	-	3^-
1357.2(2)	2.1(4)	2092.1	734.7	1^+	-
1366.4(2)	1.0(4)	2560.4	1193.8	(1^+)	-

1372.0(2)	1.6(3)	2822.1	1450.0	-	1^+
1384.3(2)	1.4(3)	2092.1	707.8	1^+	(1^+)
1386.6(2)	1.9(4)	2677.0	1290.4	1^+	-
1418.4(2)	0.8(1)	2560.4	1141.9	(1^+)	-
1427.5(2)	3.8(8)	1450.0	22.4	1^+	3^-
1503.6(3)	9.6(11)	1526.0	22.4	-	3^-
1570.2(3)	1.6(2)	2560.4	990.0	(1^+)	-
1573.5(3)	0.4(2)	2560.4	987.1	(1^+)	-
$1608.8(3)^t$	<0.2	2560.4	951.4	(1^+)	-
$1726.5(3)^t$	<0.2	2677.0	951.4	1^+	-
1825.5(3)	0.7(2)	2560.4	734.7	(1^+)	-
1834.9(3)	2.6(2)	2822.1	987.1	-	-
$1871.3(3)^t$	<0.2	2822.1	951.4	-	-
2021.8(3)	1.3(3)	2044.5	22.4	-	3^-
2378.1(3)	0.8(2)	3329.4	951.4	-	-
2428.6(3)	0.5(1)	3380.0	951.4	-	-

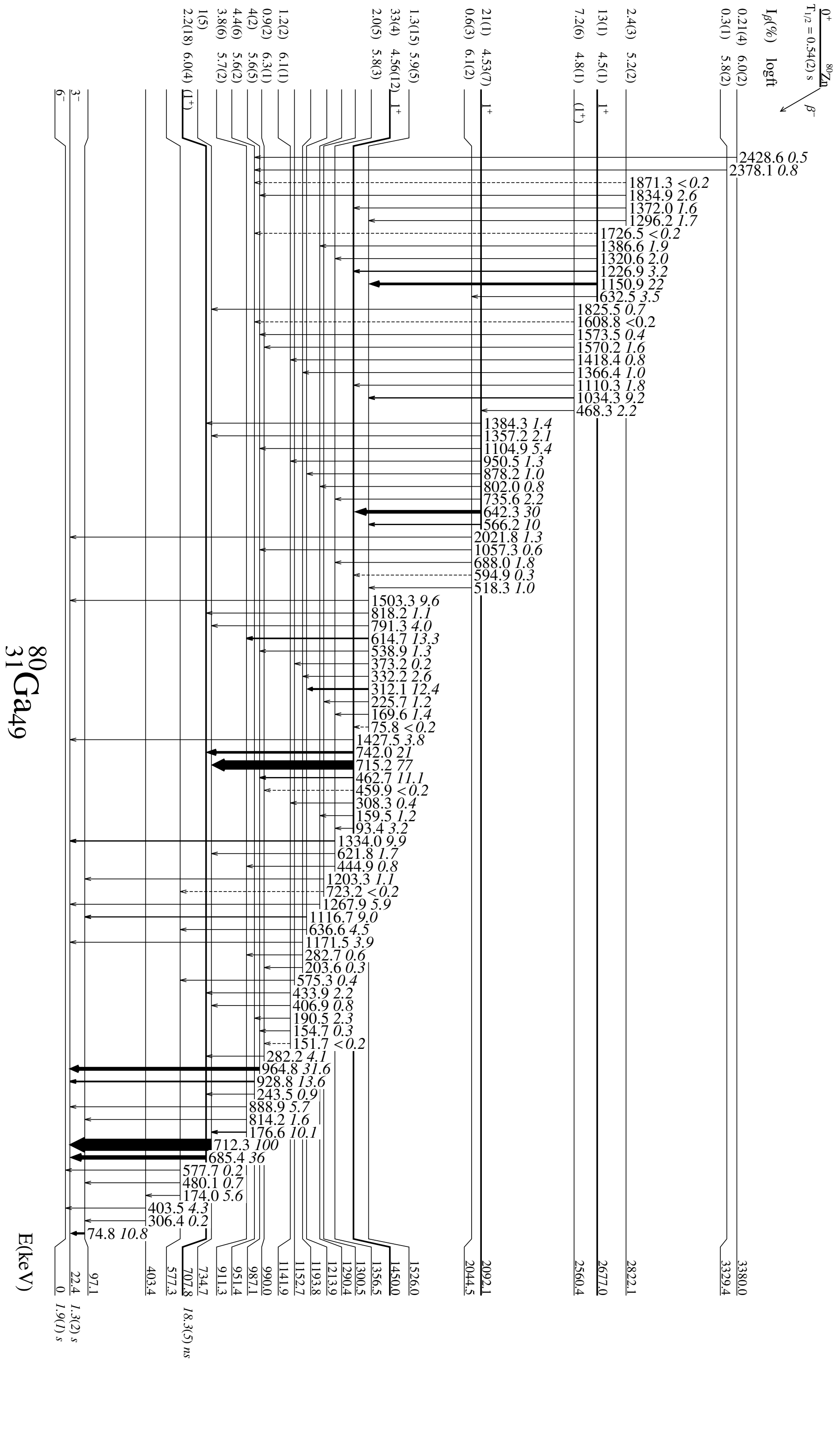

Figure 3.8: Level scheme of levels in ^{80}Ga populated in the beta decay of ^{80}Ga. There are a total of 86 gamma transitions. The dotted lines indicate tentative or weak transitions. The transition labels contain the energy value and the relative gamma intensity. For total intensity, multiply by 0.41(6).

3.3.2 Nanosecond isomer identification

The analysis of the time-difference spectra between the $LaBr_3$(Ce) detectors and the fast plastic scintillator showed a long-lived decay component which corresponds to the 685.4-keV transition, connecting the 707.8-keV and 22.4-keV 3^- levels. As shown in Fig.3.9, a gate on the 742.0 keV transition in the HPGe spectra was used to isolate the 685.4-keV transition in the $LaBr_3$(Ce) detectors.

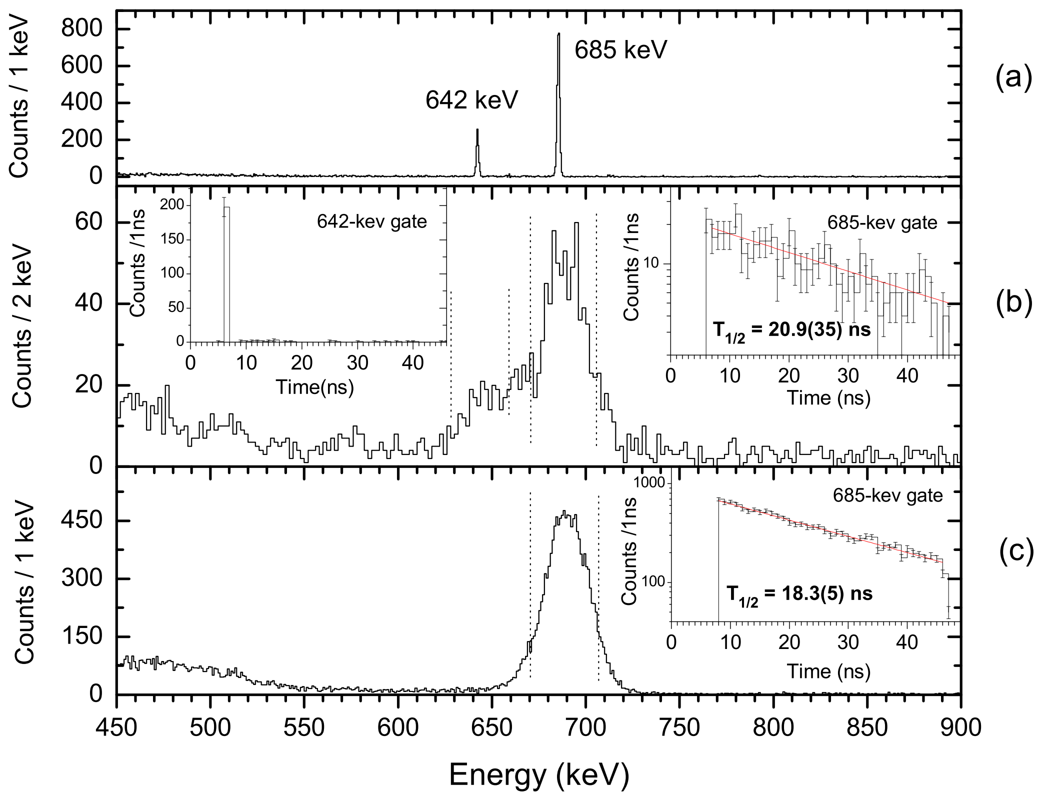

Figure 3.9: (a) 742.0 keV gate from $\gamma - \gamma$ HPGe coincidence spectra; (b) 742.0 keV gate on HPGe in the $\beta - \gamma_{(\mathrm{HPGe})} - \gamma_{(\mathrm{LaBr_3:Ce})}$ spectra. The time was recorded with Time to Amplitude Converters between the plastic scintillator (β detector) and each $LaBr_3$:(Ce) detector. The time spectra has an offset of 6 ns; (c) Delayed ($T > 8ns$) β gated spectra in $LaBr_3$:Ce.

The half-life observed, $T_{1/2} = 20.9(35)$ ns, is significantly longer than that of the prompt 642.3-keV line. It was therefore possible to completely isolate the 685.4-keV transition, by selecting only delayed $LaBr_3$(Ce) events, with respect to prompt β–$LaBr_3$(Ce) ones. Having no gating condition on the HPGe detectors provided better

Table 3.2: Comparison of reduced transition probabilities between recommended upper limits and calculations for a 686 keV transition of 18.3(5)ns half-life from a mass A=80 nucleus. We conclude that the 685.4 keV transition has M2 multipolarity and the level at 707.8 keV has $J^\pi = 1^+$.

Multipolarity	Reduced transition probability (W.u.)	
	Calculated	Limits [a]
E1	$6.2(2) \cdot 10^{-8}$	0.01
M1	$3.7(1) \cdot 10^{-6}$	3
E2	$9.9(3) \cdot 10^{-3}$	300
M2	0.60(2)	1
E3	$2.44(7) \cdot 10^{3}$	100
M3	$1.48(4) \cdot 10^{5}$	10

[a] Recommended upper limits taken from [13]

statistics and hence a more precise half-life measurement, yielding $T_{1/2} = 18.3(5)$ ns, which is the adopted value. In Table 3.2, a comparison is shown between the reduced transition probabilities for different possible multipolarities and the recommended upper limits [13]. Only an $M2$ multipolarity has a reduced transition probability of the same order of magnitude as the recommended upper limits. The very low reduced transition probabilities for an $E1$, $M1$ or $E2$ transition would suggest extremely hindered transitions, which are highly unlikely in this mass region. The $E3$ or $M3$ reduced transition probabilities are more than one and four orders of magnitude higher, respectively.

3.3.3 Conversion coefficient and multipolarity assignment for the 74.8 keV transition

The conversion coefficient for the 74.8-keV transition between the 97.1-keV and 22.4-keV levels is determined to be $\geq$0.15(18), from the intensity balance in the level scheme and with the assumption that the 97.1-keV level is not directly β fed. On the other hand, the conversion coefficient was found to be equal to 0.20(20) from the coincidence probabilities involving the 74.8-keV transition. We therefore adopt a conversion coefficient of $\leq$0.40 for the 74.8-keV γ ray. The multipolarity of this transition can therefore be assigned as $E1$ or $M1$, from a comparision with theoretical conversion coefficiencts ($\alpha(E1) = 0.15$, $\alpha(M1) = 0.15$, $\alpha(E2) = 2.08$,

$\alpha(M2) = 2.10$) [30].

3.3.4 Spin and parity assignments

The 1^+ spin and parity assignment for levels at 2677.0, 2092.1 and 1450.0 keV is based on logft values calculated for the strongly beta-fed levels. The 1^+ assignment for the 2560.0 level is only tentative.

Based on the $M2$ multipolarity of the 684 keV transition we propose a (1^+) assignment for the 707.8-keV level, even in the absence of observed strong β feeding to confirm this. This assumption is in agreement with the previous tentative assignment [27].

3.4 Comparison with Shell-Model calculations

In [16], the authors address the quenching of the Z = 28 gap around ^{78}Ni in the shell-model framework with a large valence space containing pf orbitals for protons and $pf_{5/2}g_{9/2}$ orbitals for neutrons. The calculations are able to correctly reproduce the systematics of low-lying states and magnetic moments in Cu isotopes, underlining the importance of including protons from the $f_{7/2}$ shell. It is also claimed that the $Z = 28$ shell closure is diminished when the neutron $g_{9/2}$ orbital is filled, thus pointing to the relevance of proton core excitations in order to understand the structure of neutron-rich nuclei in the vicinity of ^{78}Ni.

Honma and co-workers [31] have developed the JUN45 effective interaction for nuclei in the upper part of the pf shell. The model space used is $f_{5/2}pg_{9/2}$, including the single particle orbits $p_{3/2}$, $f_{5/2}$, $p_{1/2}$ and $g_{9/2}$.

A more recent effective interaction (jj44bpn) was developed by Brown and Lisetskiy [32] and calculations for $^{71-78}$Ga were published in [33] with the remark that for the heavier isotopes the jj44bpn interaction is quantitatively better that JUN45.

Shell-model calculations with the NuShellX@MSU code [34] were performed using the jj44bpn and JUN45 effective interactions. The calculations employ a ^{56}Ni core, and the valence protons and neutrons are allowed in the $pf_{5/2}g_{9/2}$ configuration space. In Fig. 3.10 a comparison is shown between the shell-model calculations and the present experimental results for ^{80}Ga. The calculations predict a 6^- ground state, and a group of states with spins and parities 3^-, 4^-, 5^- and 6^-, the lowest of these above 300 keV. These states are part of the $\pi f_{5/2}$-$\nu g_{9/2}$ multiplet,with the 2^- and 7^- states lying higher in energy (above 500 keV).

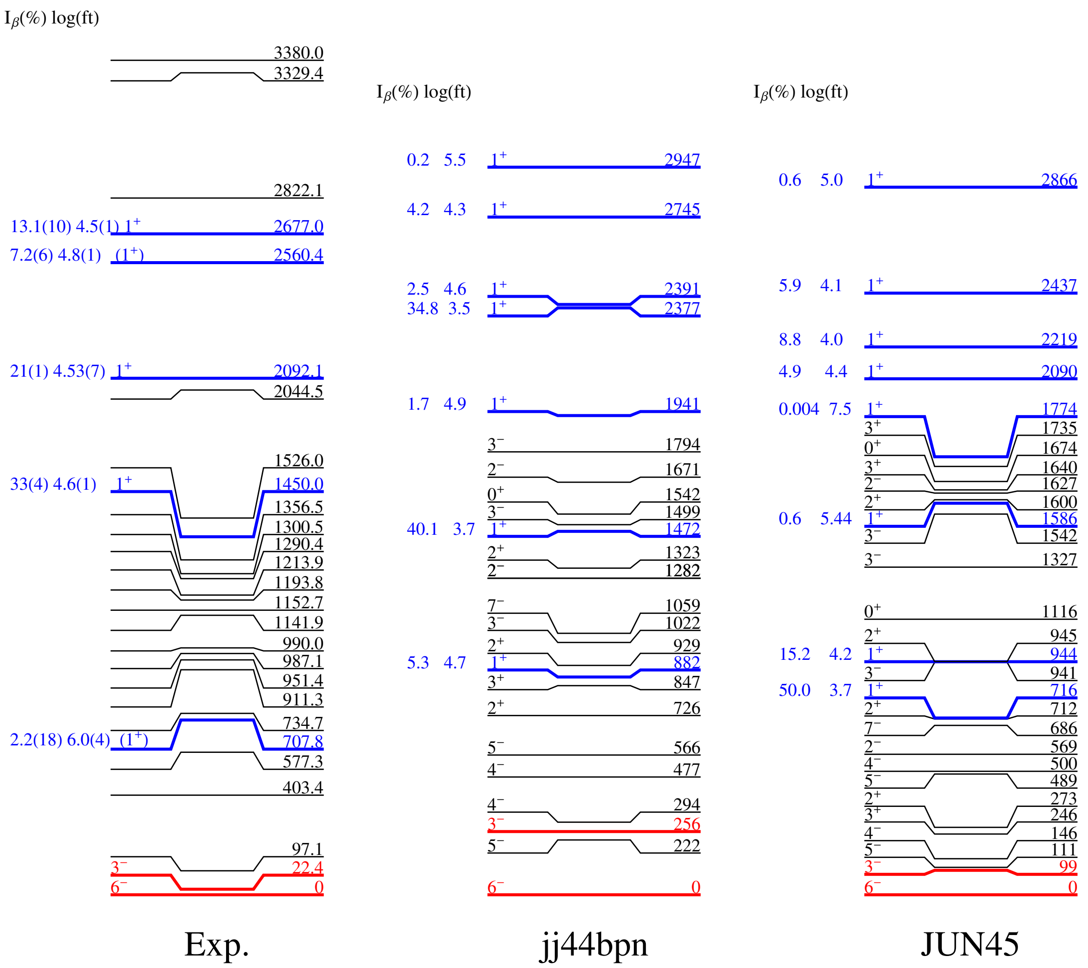

Figure 3.10: Comparison of the experimental levels (left) and shell model calculations. The experimental level scheme is the same than the one presented in Fig. 3.8. The model space used for both interactions was $p_{3/2}f_{5/2}p_{1/2}g_{9/2}$. The region $0 \rightarrow 600keV$ contains all the predicted levels. Due to high level density, regions 600 $\rightarrow$ 1800keV contain only the predicted levels with $J \leq 3$. The > 1800 keV region contains only the levels with $J^\pi = 1^+$. The experimental I_β values were measured by intensity balance between the gammas feeding and de-exciting each level.

In addition, the jj44bpn interaction provides better estimations for the both the energies and β feeding of the proposed (1^+) levels and the $B(M2)$ of the 685.4-keV transition. The latter is predicted to be 0.11 W.u. (Weisskopf units) which agrees well with the experimentally determined value of 0.6 W.u. The value calculated using the JUN45 interaction is a factor of 18 smaller. Quenched g factors of $g_s = 0.7g_{free}$ were used in these calculations, which were found in [17] to reproduce the magnetic moments of the ground states of neutron-rich Ga nuclei. The dominant configuration of the 708-keV, 1^+ level is predicted to be $\pi f^3_{5/2} \otimes \nu p^{-1}_{1/2}$ and that of the 3^- isomer $\pi f^3_{5/2} \otimes \nu g^{-1}_{9/2}$, explaining the slow nature of transitions between these two states.

In Fig. 3.10, the β-feeding intensities of states in ^{80}Ga, populated following the decay of the parent nucleus ^{80}Zn are shown. The predictions of the jj44b interaction are generaly in better agreement with the experimental data than those of the JUN45 interaction. In particular the strong β feeding of the 1^+_2 state state is well reproduced by the calculations using the jj44b interaction. The 1^+_1 state is however the strongest fed state when the JUN45 interaction is used, despite both interactions predicting similar dominant configurations for these two states.

Conclusions

The present β^- decay study brings significant new information regarding the structure of the neutron-rich $N = 49$ nucleus ^{80}Ga. The spin and parity of the ground state is firmly assigned to be 6^-, and the previously unknown excitation energy of the low-lying isomer observed by collinear laser spectroscopy [17] is now fixed at 22.4 keV. This is in agreement with the ground state assignment based on the shell-model calculations in [31, 17]. A new isomeric level with the half-life of 18.3(5) ns was observed in the present experiment, and is proposed as a candidate for the first 1^+ state. A comparison between the measured and predicted half-life of this level and the β^- feeding intensity distribution over the excited states of ^{80}Ga proved to be a sensitive test of the shell-model interactions. The predictions of the jj44bpn interaction are in a more reasonable agreement with the experimental data than the results obtained with JUN45.

The results discussed in this thesis were presented in a preliminary stage at the "Nuclear Structure and Dynamics 2012" conference which was held in Opatija, Croatia and published as conference proceedings in AIP Conf. Proc. 1491, 97 (2012). Currently, all the results are submitted to Phys. Rev. C. for publication as a regular article and are under peer-review.

Bibliography

[1] Y. Blumenfeld, T. Nilsson, and P. V. Duppen, "Facilities and methods for radioactive ion beam production," *Physica Scripta*, vol. 2013, no. T152, p. 014023, 2013. (Cited on page 1.)

[2] G. Vladuca, *Elemente de fizica nucleara, Volumul 1*. Universitatea Bucuresti: Editura Univ. din Bucuresti, 1988. (Cited on page 1.)

[3] A. Einstein, "Über einen die Erzeugung und Verwandlung des Lichtes betreffenden heuristischen Gesichtspunkt," *Annalen der Physik*, vol. 322, pp. 132–148, 1905. (Cited on page 3.)

[4] H. Geiger and E. Marsden, "On a Diffuse Reflection of the α -Particles," *Royal Society of London Proceedings Series A*, vol. 82, pp. 495–500, July 1909. (Cited on page 3.)

[5] J. Chadwick, "Possible Existence of a Neutron," *Nature*, vol. 129, p. 312, Feb. 1932. (Cited on page 4.)

[6] C. F. V. Weizsäcker, "Zur Theorie der Kernmassen," *Zeitschrift fur Physik*, vol. 96, pp. 431–458, July 1935. (Cited on page 4.)

[7] B. A. Loiseau and Y. Nogami, "Three-nucleon force," *Nuclear Physics B*, vol. 2, pp. 470–478, Aug. 1967. (Cited on page 5.)

[8] A. B. Cohen, *Concepts of Nuclear Physics*. McGraw-Hill, 1971. (Cited on page 7.)

[9] J.-L. Basdevant, M. Spiro, and J. Rich, *Fundamentals In Nuclear Physics: From Nuclear Structure to Cosmology /*. New York, NY :: Springer Science+Business Media, Inc.,, 2005. (Cited on pages 8, 22, 25 and 28.)

[10] R. F. Casten, *Nuclear structure from a simple perspective; 2nd ed.* Oxford studies in nuclear physics, Oxford: Oxford Univ. Press, 2000. (Cited on page 11.)

[11] K. S. Krane, *Introductory Nuclear Physics*. Oregon State University: John Wiley & Sons, 1988. (Cited on pages 11, 13 and 15.)

[12] R. B. Firestone, *Table of isotopes: Eight Edition*. Lawrence Berkeley National Laboratory, University of California: Wiley-Interscience, 1999. (Cited on page 23.)

[13] P. Endt, "Strengths of gamma-ray transitions in $A = 45 - 90$ nuclei," *Atomic Data and Nuclear Data Tables*, vol. 23, no. 6, pp. 547–585, 1979. (Cited on pages 23 and 44.)

[14] W. E. Meyerhof, *Elements of Nuclear Physics*. Stanford University: McGraw-Hill, 1967. (Cited on page 29.)

[15] J. Hakala, S. Rahaman, V.-V. Elomaa, T. Eronen, U. Hager, A. Jokinen, A. Kankainen, I. D. Moore, H. Penttilä, S. Rinta-Antila, J. Rissanen, A. Saastamoinen, T. Sonoda, C. Weber, and J. Äystö, "Evolution of the $N = 50$ shell gap energy towards ^{78}Ni," *Phys. Rev. Lett.*, vol. 101, p. 052502, Jul 2008. (Cited on page 31.)

[16] K. Sieja and F. Nowacki, "Shell quenching in ^{78}Ni: A hint from the structure of neutron-rich copper isotopes," *Phys. Rev. C*, vol. 81, p. 061303, Jun 2010. (Cited on pages 31 and 45.)

[17] B. Cheal, J. Billowes, M. L. Bissell, K. Blaum, F. C. Charlwood, K. T. Flanagan, D. H. Forest, S. Fritzsche, C. Geppert, A. Jokinen, M. Kowalska, A. Krieger, J. Krämer, E. Mané, I. D. Moore, R. Neugart, G. Neyens, W. Nörtershäuser, M. M. Rajabali, M. Schug, H. H. Stroke, P. Vingerhoets, D. T. Yordanov, and M. Žáková, "Discovery of a long-lived low-lying isomeric state in ^{80}Ga," *Phys. Rev. C*, vol. 82, p. 051302, Nov 2010. (Cited on pages 31, 36, 37, 47 and 49.)

[18] D. Verney, B. Tastet, K. Kolos, F. Le Blanc, F. Ibrahim, M. Cheikh Mhamed, E. Cottereau, P. V. Cuong, F. Didierjean, G. Duchêne, S. Essabaa, M. Ferraton, S. Franchoo, L. H. Khiem, C. Lau, J.-F. Le Du, I. Matea, B. Mouginot, M. Niikura, B. Roussière, I. Stefan, D. Testov, and J.-C. Thomas, "Structure of ^{80}Ge revealed by the beta decay of isomeric states in ^{80}Ga: Triaxiality in the vicinity of ^{78}Ni," *Phys. Rev. C*, vol. 87, p. 054307, May 2013. (Cited on page 32.)

[19] "Laboratory portrait: The ISOLDE facility," *Nuclear Physics News International*, vol. 20, no. 4, 2010. (Cited on page 32.)

[20] U. Köster, T. Behrens, C. Clausen, P. Delahaye, V. N. Fedoseyev, L. M. Fraile, R. Gernhäuser, T. J. Giles, A. Ionan, T. Kröll, H. Mach, B. Marsh, M. Seliverstov, T. Sieber, E. Siesling, E. Tengborn, F. Wenander, and J. van de Walle, "ISOLDE beams of neutron-rich zinc isotopes: yields, release, decay spectroscopy," vol. 798, pp. 315–326, Nov. 2005. (Cited on page 33.)

[21] E. Bouquerel, R. Catherall, M. Eller, J. Lettry, S. Marzari, T. Stora, and I. Collaboration, "Purification of a Zn radioactive ion beam by alkali suppression in

a quartz line target prototype," *The European Physical Journal Special Topics*, vol. 150, no. 1, pp. 277–280, 2007. (Cited on page 33.)

[22] U. Köster, O. Arndt, E. Bouquerel, V. N. Fedoseyev, H. Frånberg, A. Joinet, C. Jost, I. S. K. Kerkines, R. Kirchner, and Targisol Collaboration *Nuclear Instruments and Methods in Physics Research B*, vol. 266, pp. 4229–4239, 2008. (Cited on pages 33 and 34.)

[23] Y. Blumenfeld, T. Nilsson, and P. V. Duppen, "Facilities and methods for radioactive ion beam production," *Physica Scripta*, vol. 2013, no. T152, p. 014023, 2013. (Cited on page 33.)

[24] H. Mach, R. Gill, and M. Moszynski, "A method for picosecond lifetime measurements for neutron-rich nuclei," *Nuclear Instruments and Methods in Physics Research Section A: Accelerators, Spectrometers, Detectors and Associated Equipment*, vol. 280, no. 1, pp. 49 – 72, 1989. (Cited on page 34.)

[25] M. Moszynski and H. Mach, "A method for picosecond lifetime measurements for neutron-rich nuclei: Timing study with scintillation counters," *Nuclear Instruments and Methods in Physics Research Section A*, vol. 277, no. 2-3, 1989. (Cited on page 34.)

[26] X. LLC, *User's Manual - Digital Gamma Finder (DGF) Pixie-4*. 31057 Genstar Road Hayward, CA 94544 USA: XIA, 2011. (Cited on page 34.)

[27] J. A. Winger, J. C. Hill, F. K. Wohn, R. Moreh, R. L. Gill, R. F. Casten, D. D. Warner, A. Piotrowski, and H. Mach, "Decay of ^{80}Zn: Implications for shell structure and r -process nucleosynthesis," *Phys. Rev. C*, vol. 36, pp. 758–764, Aug 1987. (Cited on pages 36 and 45.)

[28] B. Ekström, B. Fogelberg, P. Hoff, E. Lund, and A. Sangariyavanish, "Decay properties of $^{75-80}$Zn and Q_β-values of neutron-rich Zn and Ga isotopes," *Physica Scripta*, vol. 34, no. 6A, p. 614, 1986. (Cited on page 36.)

[29] A. Makishima, M. Asai, T. Ishii, I. Hossain, M. Ogawa, S. Ichikawa, and M. Ishii *Phys. Rev. C*, vol. 59, pp. R2331–R2333, May 1999. (Cited on page 37.)

[30] T. Kibédi and T.W. Burrows and M.B. Trzhaskovskaya and P.M. Davidson and C.W. Nestor Jr., "Evaluation of theoretical conversion coefficients using bricc," *Nuclear Instruments and Methods in Physics Research Section A: Accelerators, Spectrometers, Detectors and Associated Equipment*, vol. 589, no. 2, pp. 202–229, 2008. (Cited on page 45.)

[31] M. Honma, T. Otsuka, T. Mizusaki, and M. Hjorth-Jensen, "New effective interaction for $f5pg9$-shell nuclei," *Phys. Rev. C*, vol. 80, p. 064323, Dec 2009. (Cited on pages 45 and 49.)

[32] B. Brown and A. Lisetskiy *Unpublished*. (Cited on page 45.)

[33] P. C. Srivastava, "Structure of $^{71-78}$Ga isotopes in the $f_{5/2}$ $pg_{9/2}$ and $fpg_{9/2}$ spaces," *Journal of Physics G: Nuclear and Particle Physics*, vol. 39, no. 1, p. 015102, 2012. (Cited on page 45.)

[34] B. A. Brown, W. D. M. Rae, E. McDonald and M. Horoi, "NuShellX@MSU," in *http://www.nscl.msu.edu/~brown/resources/resources.html* (http://www.garsington.eclipse.co.uk, ed.), NuShellX, W. D. M. Rae. (Cited on page 45.)